Theses and Dissertations   1. Thesis and Dissertation Collection, all items

2015-09

Direction finding using multiple MEMS acoustic sensors

Wilmott, Daniel

Monterey, California: Naval Postgraduate School

http://hdl.handle.net/10945/47345

NAVAL POSTGRADUATE SCHOOL

MONTEREY, CALIFORNIA

THESIS

DIRECTION FINDING USING MULTIPLE MEMS ACOUSTIC SENSORS

by

Daniel Wilmott

September 2015

Thesis Advisor: Gamani Karunasiri
Co-Advisor: Fabio Alves

Approved for public release; distribution is unlimited

THIS PAGE INTENTIONALLY LEFT BLANK

REPORT DOCUMENTATION PAGE	*Form Approved OMB No. 0704-0188*

Public reporting burden for this collection of information is estimated to average 1 hour per response, including the time for reviewing instruction, searching existing data sources, gathering and maintaining the data needed, and completing and reviewing the collection of information. Send comments regarding this burden estimate or any other aspect of this collection of information, including suggestions for reducing this burden, to Washington headquarters Services, Directorate for Information Operations and Reports, 1215 Jefferson Davis Highway, Suite 1204, Arlington, VA 22202-4302, and to the Office of Management and Budget, Paperwork Reduction Project (0704-0188) Washington DC 20503.

1. AGENCY USE ONLY *(Leave blank)*	2. REPORT DATE September 2015	3. REPORT TYPE AND DATES COVERED Master's thesis	
4. TITLE AND SUBTITLE DIRECTION FINDING USING MULTIPLE MEMS ACOUSTIC SENSORS			**5. FUNDING NUMBERS**
6. AUTHOR(S) Wilmott, Daniel			
7. PERFORMING ORGANIZATION NAME(S) AND ADDRESS(ES) Naval Postgraduate School Monterey, CA 93943-5000			**8. PERFORMING ORGANIZATION REPORT NUMBER**
9. SPONSORING /MONITORING AGENCY NAME(S) AND ADDRESS(ES) N/A			**10. SPONSORING / MONITORING AGENCY REPORT NUMBER**

11. SUPPLEMENTARY NOTES The views expressed in this thesis are those of the author and do not reflect the official policy or position of the Department of Defense or the U.S. Government. IRB Protocol number ____N/A____.

12a. DISTRIBUTION / AVAILABILITY STATEMENT Approved for public release; distribution is unlimited	12b. DISTRIBUTION CODE

13. ABSTRACT (maximum 200 words)

A microelectromechanical direction-finding sensor has been developed based on the mechanically coupled ears of the *Ormia ochracea* fly. Previous designs determined the direction of sound relative to the normal of the sensor by using the sound pressure level at the sensor. However, these designs suffered from a left-right ambiguity. To overcome these shortcomings, a dual sensor assembly was created. Two sensors co-located at an offset angle allow direction finding across 120°. This eliminated ambiguous angles and the requirement for a sound pressure level.

For this study, the dual sensor assembly was fabricated using two custom circuit boards powered by a 9V battery and arranged on a 3D-printed mount. The resonant frequency of the sensors produced a 260 V/Pa output at 1.690 kHz ± 20 Hz. Experimental work was done in an anechoic chamber, and outputs were captured using lock-in amplifiers. The angle error ranged from less than 0.3° close to the normal axis (0°) to 3.4° at the limits of coverage, ± 60°. The outcome of this research is that it is possible to operate this microelectromechanical direction-finding sensor assembly to find the bearing of a signal on resonance over an angular range of 120° with a maximum uncertainty of 3.4°.

14. SUBJECT TERMS MEMS, direction finding, *Ormia ochracea*, acoustic sensor, coupled oscillator			**15. NUMBER OF PAGES** 77
			16. PRICE CODE
17. SECURITY CLASSIFICATION OF REPORT Unclassified	**18. SECURITY CLASSIFICATION OF THIS PAGE** Unclassified	**19. SECURITY CLASSIFICATION OF ABSTRACT** Unclassified	**20. LIMITATION OF ABSTRACT** UU

THIS PAGE INTENTIONALLY LEFT BLANK

DIRECTION FINDING USING MULTIPLE MEMS ACOUSTIC SENSORS

Daniel Wilmott
Lieutenant Commander, Royal Canadian Navy
B. Eng., Royal Military College, 2004

Submitted in partial fulfillment of the
requirements for the degree of

MASTER OF SCIENCE IN ENGINEERING ACOUSTICS

from the

NAVAL POSTGRADUATE SCHOOL
September 2015

Approved by: Gamani Karunasiri
                      Thesis Advisor

                      Fabio Alves
                      Co-Advisor

                      Daphne Kapolka
                      Chair, Engineering Acoustics Academic Committee

THIS PAGE INTENTIONALLY LEFT BLANK

ABSTRACT

A microelectromechanical direction-finding sensor has been developed based on the mechanically coupled ears of the *Ormia ochracea* fly. Previous designs determined the direction of sound relative to the normal of the sensor by using the sound pressure level at the sensor. However, these designs suffered from a left-right ambiguity. To overcome these shortcomings, a dual sensor assembly was created. Two sensors co-located at an offset angle allow direction finding across 120°. This eliminated ambiguous angles and the requirement for a sound pressure level.

For this study, the dual sensor assembly was fabricated using two custom circuit boards powered by a 9V battery and arranged on a 3D-printed mount. The resonant frequency of the sensors produced a 260 V/Pa output at 1.690 kHz ± 20 Hz. Experimental work was done in an anechoic chamber, and outputs were captured using lock-in amplifiers. The angle error ranged from less than 0.3° close to the normal axis (0°) to 3.4° at the limits of coverage, ± 60°. The outcome of this research is that it is possible to operate this microelectromechanical direction-finding sensor assembly to find the bearing of a signal on resonance over an angular range of 120° with a maximum uncertainty of 3.4°.

THIS PAGE INTENTIONALLY LEFT BLANK

TABLE OF CONTENTS

THIS PAGE INTENTIONALLY LEFT BLANK

LIST OF FIGURES

LIST OF TABLES

THIS PAGE INTENTIONALLY LEFT BLANK

ACKNOWLEDGMENTS

This innovative project of direction finding using a sensor based on a fly's ear has been very interesting and rewarding. Many people worked on this project before me, and there will be more who contribute to it in the future. Mike Touse did some fantastic work for his Ph.D. dissertation that has continually been a reference for those of us who came after him. Steve Harrison, a fellow Canadian, gave me the first glimpse of this project before I even came to NPS. John Roth's contribution on the capacitive readout allowed me to use a convenient chip that is no longer supported by the company who makes it.

My advisors, Dr. Gamani Karunasiri and Dr. Fabio Alves, have been an ideal team who continually helped me through the project. Thank you, Dr. Karunasiri, for your quiet confidence in me, motivation to get something accomplished each week and your infectious enthusiasm. Dr. Alves, you have been a fantastic support in the lab. You sacrificed so much of your own time to keep me on track and were truly invested in my learning. Because you tirelessly supported me, you knew instinctively when I needed rescuing and perhaps, more importantly, when I had done enough. Thank you.

To the many professors and technical staff in the Physics and Electrical Engineering Departments whom I had the pleasure of being led by, thank you. Please continue your good work, so that military men and women around the world continue to receive such an education.

To my wife, Andrea, and children, Abigail and Noah, thank you for your unending patience and confidence in me and the countless ways you have sacrificed and supported me to get here. I could not hope for anything more. Any degree, memory, or success that comes from our California adventure is equally shared with all of you.

THIS PAGE INTENTIONALLY LEFT BLANK

I. INTRODUCTION

A. BACKGROUND

In 1776 the physicist J. B. Venturi, most widely known for his work in fluid dynamics, surmised that the ability to find the direction of a sound source was based on the amplitude difference between two ears [1]. Lord Rayleigh confirmed this in 1907 by concluding that the different distances sound traveled to each ear resulted in a phase difference for periodic sound waves, which is detected by an amplitude difference [2]. In animals with a relatively large ear separation compared to the sound wavelength, the delay of the sound arrival, inter-aural time difference (ITD), and variation in the pressure field between ears, inter-aural level difference (ILD), allows for direction finding (DF). Humans use this principle to determine sound direction with up to 2 degree accuracy [3]. This study explores a novel approach to direction finding also found in nature, the parasitic fly *Ormia ochracea*.

1. The *Ormia Ochracea*

The *Ormia ochracea* fly is particularly adept at direction finding a sound source. However, because of its small size, something more must be taking place. The female of this species seek out chirping crickets to lay their eggs on, and do so with an accuracy of less than 2 degrees. The two eardrums of the fly are separated by a mere 1.5 mm, yet it homes in on the cricket chirping with a 7 cm wavelength, using an ITD of at most 2.5 μs and negligible ILD [4].

Figure 1   *Ormia ochracea* ears and corresponding mechanical model.
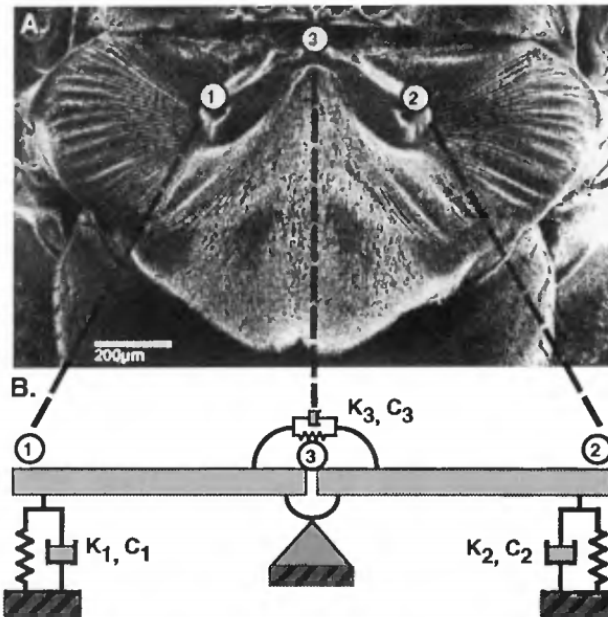
Each ear is modeled as a rigid bar with damping and spring constants. The intertympanal bridge is a pivot with similar damping and spring constants. This allows for relatively simple transfer functions to describe system operation in the steady state during sound excitation. From [4].

Shown in Figure 1, the fly's ears consist of two thin hardened membranes, *prosternal tympanal membranes,* each of which has a stiff rod coupling their movement to a pair of auditory sensing organs, the *bulbae acusticae*, inside the head. These membranes are connected together at the center of the head by a bridge known as the *intertympanal bridge*. In Figure 1 these structures are shown and have been modeled by a dual cantilever arrangement that incorporates the damping of both tympanal membranes and the intertympanal bridge. "In effect, the mechanical system expands the interaural amplitude and time differences. This results from its sensitivity to the difference between the forces on the two sides of the ear. … Because the intertympanal bridge pivots about its center, the system is very sensitive to the difference in these forces [4]."

Miles et al. [4] go on to confirm that this mechanical model sufficiently captures the important motion of the *Ormia ochracea* ear and show that the ears have two natural resonant frequencies. In the first mode the ears move out of phase with each other in a pure rocking mode. This rocking mode is a result of the difference between the forces on

each ear. The second mode has the ears moving identically and in phase, resulting in a pure bending mode about the tympanal bridge. The bending mode is a result of the sum of the forces on the ears. These modes, caused by the mechanical link between eardrums, give the *Ormia ochracea* "remarkable sensitivity to the direction of an incident sound stimulus [4]."

It is reasonable to expect that the bending mode produces greater displacement of the ears, because it is the result of a sum of the forces. Also, because this is a resonant response, the signal to noise ratio (SNR) of the sensor is inherently better than a sensor that takes stimulus from a wider range of frequencies.

2. The Size Advantage

Capitalizing on the bending mode of this coupled ear system leads to sensors that are significantly smaller than traditional microphone DF systems (see Chapter I.A.3). Smaller sensors use very little power and can be installed in many places without disruption to the environment or other equipment. Multiple sensors can be installed in varying locations to allow for greater coverage and survivability over single systems of interconnected microphones. More sensors with low power requirements and simple interface protocols will be easily incorporated into information management and display systems.

Due to their small size, fabrication is done using microelectromechanical (MEM) techniques. This approach allows the production of many identical sensors with high fidelity to the design, allowing the resonant frequency range to be controlled reliably.

3. Existing Acoustic DF Technology

Direction finding of sounds is not a new challenge. Companies such as Raytheon and Qinetiq sell devices aimed at detecting the source of incoming gunfire. Raytheon BBN Technologies offers the Boomerang System shown in Figure 2 and Figure 3.

Figure 2   Raytheon BBN Technologies Boomerang III.

Intended to be mounted on a vehicle or building, the Boomerang III uses multiple microphones to detect incoming fire of plus or minus 15 degrees. (From [5])

Figure 3   Raytheon BBN Technologies Boomerang Warrior-X.

A shoulder-mounted device detects incoming fire and provides visual and/or audio announcement via speaker, earpiece or lightweight display with an accuracy of plus or minus 15 degrees. (From [6])

Boomerang units … use seven small microphones, arranged like the spine of a sea urchin, to detect both the muzzle blast and the shock wave from a speeding bullet. Once a sniper's bullet is detected, Boomerang's display panel, which is located inside the vehicle, alerts soldiers through an LED 12-hour clock image display panel and speaker mounted inside the vehicle that a bullet has been fired, and gives its direction and elevation. The system resets for subsequent shot detection. [7]

According to unclassified information found at [5], [7] and [8], the Boomerang system provides shooter direction to plus or minus 15 degrees within 2 seconds for shot miss distances of 1 to 30 m for shots taken up to ¼ mile away.

Qinetiq offers a similar system to the Boomerang, the EARS Gunshot Localization system. The shoulder mounted version utilizes four acoustic detectors to locate incoming fire and weighs between 0.45 and 0.9 kg [9], [10]. The system is also available in vehicle mounted and stationary versions. Visually the shoulder-mounted version looks remarkably similar in size (472 cc) and placement to the Boomerang Warrior-X (Figure 4).

Figure 4   Qinetiq EARS Gunshot Localization system.

This shoulder-mounted version runs on two CR123 li-ion batteries for up
to 14 hours and provides voice and visual alerts with an accuracy of plus
or minus 7.5 degrees. (From [9]).

Qinetiq documentation boasts an accuracy of plus or minus 7.5 degrees bearing accuracy within < 1 second with detection ranges greater than 400 m. Output is provided through audio or visual interfaces (e.g., 3 o'clock, 400 meters) [9].

4.   Previous Work at NPS

Touse et al. [11] have demonstrated a microelectromechanical system (MEMS) directional sound sensor based on the fly's eardrums. Fabrication of sensors was performed by MEMSCAP®, a commercial foundry specializing in Silicon-on-Insulator Multi User Manufacturing Process (SOIMUMPS) [12]. In their process, the SOI substrate thickness is 400 μm with a 25 μm-thick device layer, and etching is available on both sides of the SOI wafer that results in a 25 μm device with a trench on the back. The sensor was operated at the bending frequency due to its large amplitude of vibration. Because the bending mode is excited by the pressure gradient of the sound, the sensor

acts as a pressure gradient microphone with an amplitude, which demonstrates a cosine dependence to the direction of sound.

The previous work with single sensors used a spherical coordinate system (Figure 5) where the bending plates corresponding to the fly's ears lay in the xy plane, and the hinge between the plates was in the y-direction. All measurements were taken using sources located in the xz plane by varying the polar angle θ and thus using azimuth angles of $\varphi = 0°$ or $\varphi = 180°$.

Figure 5   Spherical coordinates.
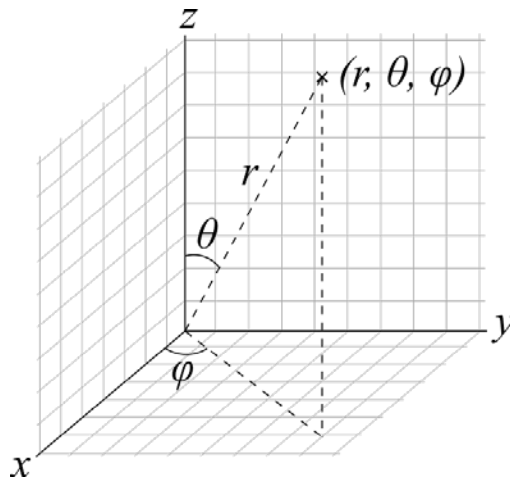
During this study it should be considered that the sensor being evaluated is located at the origin of a spherical coordinate system with the z-axis normal to the sensor face. Incoming sound is measured at varying angles of θ while maintaining $\varphi = 0°$ or $\varphi = 180°$. (From [13]).

Since the first generation of sensors was developed, 11 further iterations of the design have been produced to refine the design. Highly sensitive comb fingers have been added and optimized to improve the sensor readout [14]. The sensor dimensions can be adjusted to result in a resonant frequency between 1 and 20 kHz. All generations have been based on the design shown in Figure 6.

Figure 6   Early generation MEMS acoustic DF sensor.

(wing) (bridge) (leg)
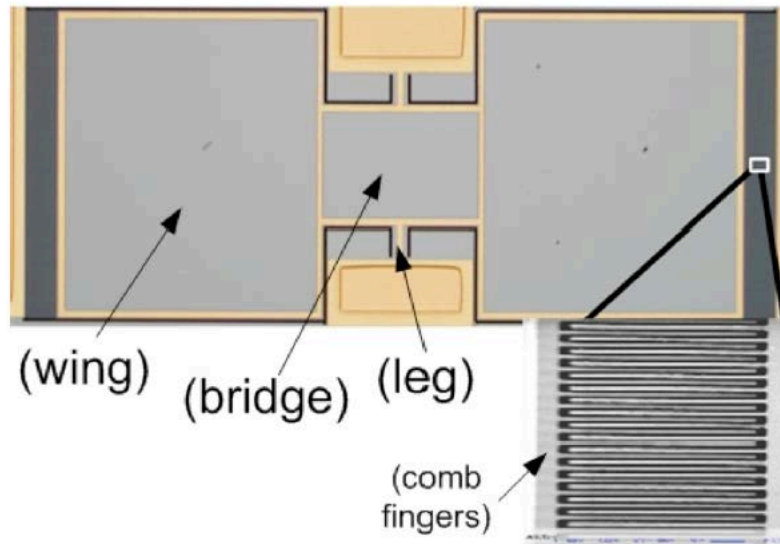
(comb fingers)

Photo of first-generation MEMS sensor showing the wings, bridge, and legs used to replicate the *Ormia ochracea* in a Si substrate. Inter-digitated comb finger capacitors on the outer edge of the wings provide the mechanism to detect wing movement through varying capacitance as the comb fingers move relative to each other. (From [11]).

The sensors use capacitive comb fingers to produce an electrical output proportional to wing displacement. M. Touse showed that, as the wings of the sensor move relative to the substrate, an external electronic circuit could be used to sense the corresponding change in capacitance and amplify the resulting voltage [11]. J. Roth determined that an unpackaged die of Irvine Sensors' Universal Capacitive Readout IC (MS3110) is suitable for this purpose [15]. A demonstration version of a sensor, stabilizing capacitors, and the MS3110 is pictured in Figure 7.

Figure 7   Previous generation sensor.
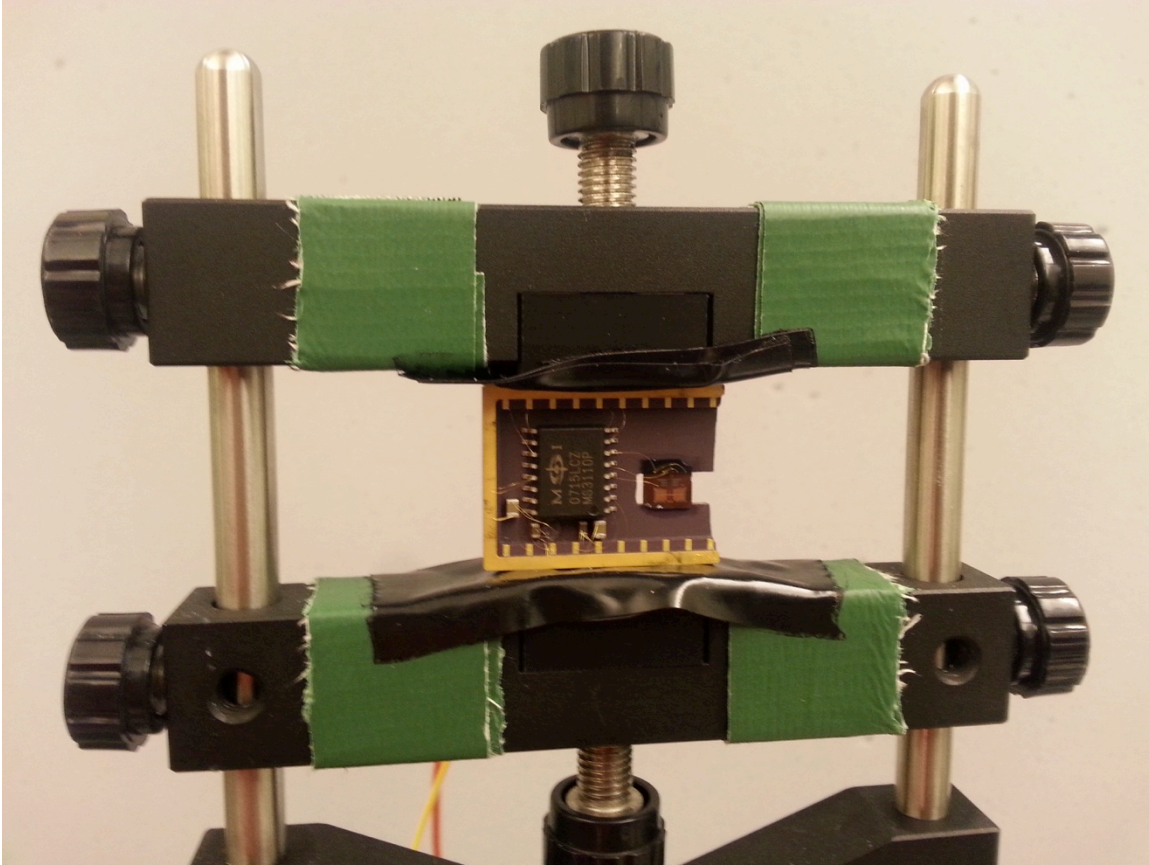
A previous generation sensor made on a ceramic hybrid mounting package. The MEMS DF sensor is located on the right side, with the MS3110 readout chip and stabilizing capacitors on the left. All connections between the readout, sensor, and interface lines are wirebonded. Individual wires on the back of the package provide programming and output interface. Fabrication and use are possible but are delicate and cumbersome.

The sensor has a predictable response to excitation at the bending resonant frequency as shown in Figure 8 and represented by:

$$P = \left| \alpha P_o \cos(\theta) \right| \qquad (1)$$

where P is the sensor readout output, α is a normalization constant applied according to sensor baseline readings, P_o is the amplitude of the incoming sound pressure, and θ is the direction of arrival. In order to independently predict the incoming sound direction, the sound pressure at the source must be known.

Figure 8   Measured and theoretical responses of a single sensor.
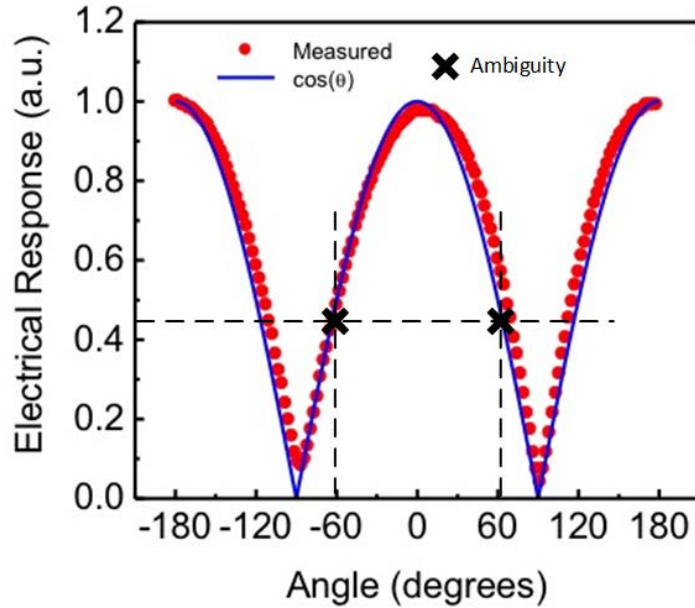
The measured output follows a cosine dependence that can be used to determine incident angle from a given sensor output. An angle ambiguity exists on either side of 0° (normal incidence) where the same sensor output occurs for both azimuthal angles in the xz-plane. (After [11]).

Furthermore, there is an ambiguity mirrored across the normal axis of the device as shown in Figure 8. The *Ormia ochracea* fly solves the problem of ambiguity by coupling the rocking and bending modes to generate two different vibrational amplitudes at the two eardrums [4]. However, despite the efforts to date, practical use of the rocking mode is yet to be realized by properly coupling the two modes. One attractive way to solve both the angular ambiguity and the requirement to know the sound pressure is to use multiple sensors.

B.   OBJECTIVE AND THESIS ORGANIZATION

In the context of the previous section. the objective of this thesis is to continue development of a MEMS DF sensor system by integrating two sensors with more robust readout circuitry and optimize the system for high resolution sound direction detection.

This thesis is an important step in achieving the goal of the project proposed at [16]:

> To develop an acoustic direction finding (DF) system for sniper fire detection based on a recently developed MEMS directional microphone that mimics the ears of the fly *Ormia ochracea*. The resonant excitation employed in the detection enhances the S/N compared to omni-directional microphones used in current DF systems. This translates into enhanced direction finding accuracy.

This thesis is organized into four chapters. Chapter I gave an introduction of the overall project that this thesis supports, the previous work conducted, and the genesis of the sensor being designed. Chapter II details the theory of direction finding using multiple sensors. This is how the aforementioned angular ambiguity and requirement to measure source level will be avoided by concurrent processing of two sensors' outputs.

Chapter III contains descriptions, diagrams, and troubleshooting details associated with verifying the theoretical approach of Chapter II in an anechoic chamber. Details of creating sensors based on commercially fabricated printed circuit boards (PCBs), 3D-printed sensor mounts, sensor calibration, and anechoic chamber setup are included.

Chapter IV contains the results of testing in the NPS anechoic chamber. Chapter V provides an assessment of the experimental results, discussion on the relative success of the work done, and recommendations for further work.

All references to decibel measurements use the standard reference pressure level in air, 20 µPa.

THIS PAGE INTENTIONALLY LEFT BLANK

II.   DIRECTION FINDING USING MULTIPLE SENSORS

A single DF sound sensor in the bending mode performs adequately to provide the polar angle in a 90° range; however, as shown in Figure 8, the azimuthal angle cannot be determined. In addition, to properly resolve the polar angle using (1), the source level P_o must be known. Two DF sensors arranged as per Figure 9 to form a dual sensor assembly can solve these challenges with minimal post-processing. In this case, the xy-plane of the coordinate system used to define the angles is oriented along the red substrate holding the sensors. Again, the y-axis runs in the direction of the hinges between the plates, and measurements are taken by varying the polar angle in the xz-plane.

Figure 9   Arrangement of multiple MEMS DF sensors.
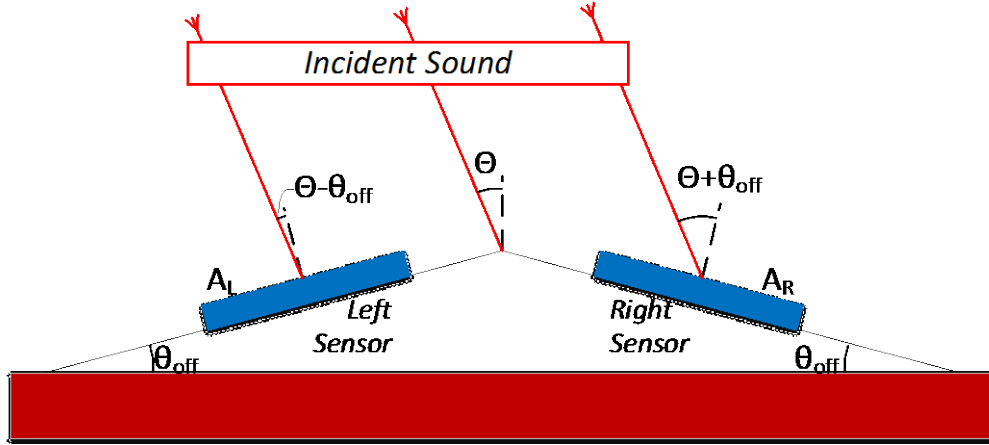
In this arrangement, two sensors are co-located at an angle θ_{off} such that the incident sound will interact at $\theta - \theta_{off}$ at the left sensor and $\theta + \theta_{off}$ at the right sensor. This will provide an effective coverage of θ from $-90+\theta_{off}$ to $+90-\theta_{off}$ with no angle ambiguity or requirement to measure the incoming sound level. (From [17]).

Because each sensor produces an output (P) cosine dependence as in (1) and both are symmetrically positioned at an offset angle θ_{off}, the azimuthal angle ambiguity in the xz-plane can be resolved. Both sensors are co-located in close proximity to each other, such that the amplitude of sound pressure can be considered nearly the same at both

sensors. Applying (1) to the left (index L) and right (index R) sensors, the pressure experienced by the two sensors can be written as:

$$P_L = P_o \cos(\theta - \theta_{off}), \ -90° + \theta_{off} \leq \theta \leq 90° - \theta_{off} \tag{2}$$

$$P_R = P_o \cos(\theta + \theta_{off}), \ -90° + \theta_{off} \leq \theta \leq 90° - \theta_{off} \tag{3}$$

Combining the difference and sum of both returns allows for cancellation of the source level and resolution of angle ambiguity.

$$\frac{P_L - P_R}{P_L + P_R}$$
$$\frac{P_o \cos(\theta - \theta_{off}) - P_o \cos(\theta + \theta_{off})}{P_o \cos(\theta - \theta_{off}) + P_o \cos(\theta + \theta_{off})}$$
$$\frac{P_o}{P_o} \left(\frac{\cos(\theta - \theta_{off}) - \cos(\theta + \theta_{off})}{\cos(\theta - \theta_{off}) + \cos(\theta + \theta_{off})} \right), \ -90° + \theta_{off} \leq \theta \leq 90° - \theta_{off} \tag{4}$$

The use of common trigonometric identities simplifies this to:

$$\frac{P_L - P_R}{P_L + P_R} = \tan(\theta_{off}) \tan(\theta) \tag{5}$$

which can be readily solved in terms of the known quantities of a received sound:

$$\theta = \tan^{-1} \left(\frac{1}{\tan(\theta_{off})} \frac{P_L - P_R}{P_L + P_R} \right), \ -90° + \theta_{off} \leq \theta \leq 90° - \theta_{off} \tag{6}$$

Because the sensor output measures the magnitude of the wing displacement, equation (1) relies on the absolute value of cosine. This absolute value propagates through the calculations leading to (4) as a limitation on the angles it is valid for, $\theta = \pm 60°$ when $\theta_{off} = 30°$ [17].

Figure 10 shows the theoretical normalized response of two individual sensors arranged with an offset angle of $\theta_{off} = 30°$ as illustrated in Figure 9.

Figure 10   Theoretical response of two sensors.
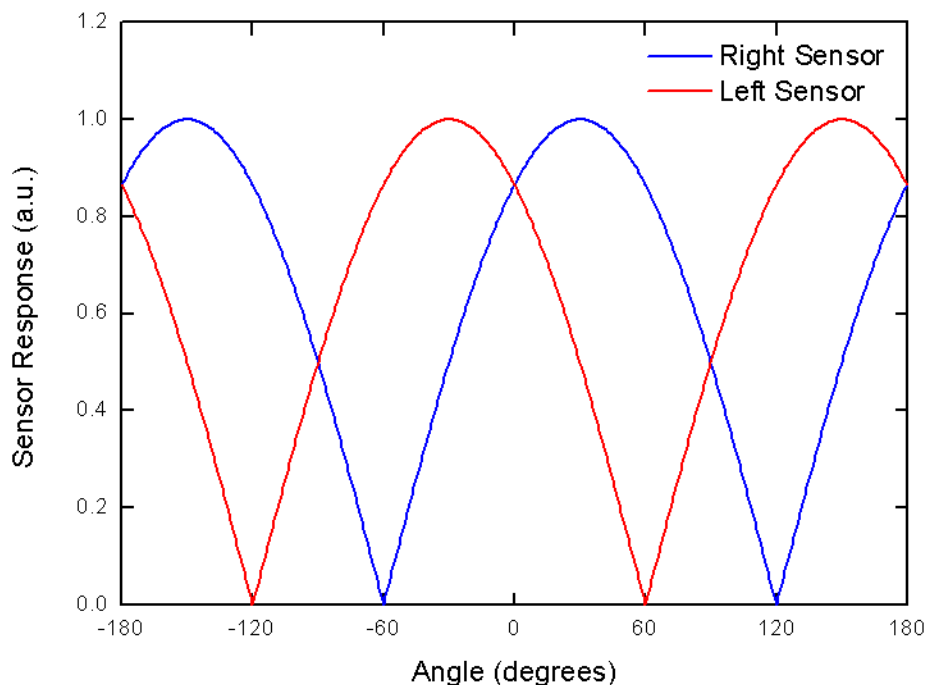
Theoretical normalized response of two individual sensors arranged with an offset angle of $\theta_{off} = 30°$. This will give unambiguous sensor outputs across a range of $\theta = \pm 60°$ from normal incidence.

Figure 11 shows the theoretical direction of arrival and the corresponding sensor response when calculated as the difference divided by the sum of individual sensor outputs. This matches the left side of (5) and offers unambiguous direction finding between $\pm 60°$ from normal incidence.

Figure 11   Difference divided by sum of sensor outputs.
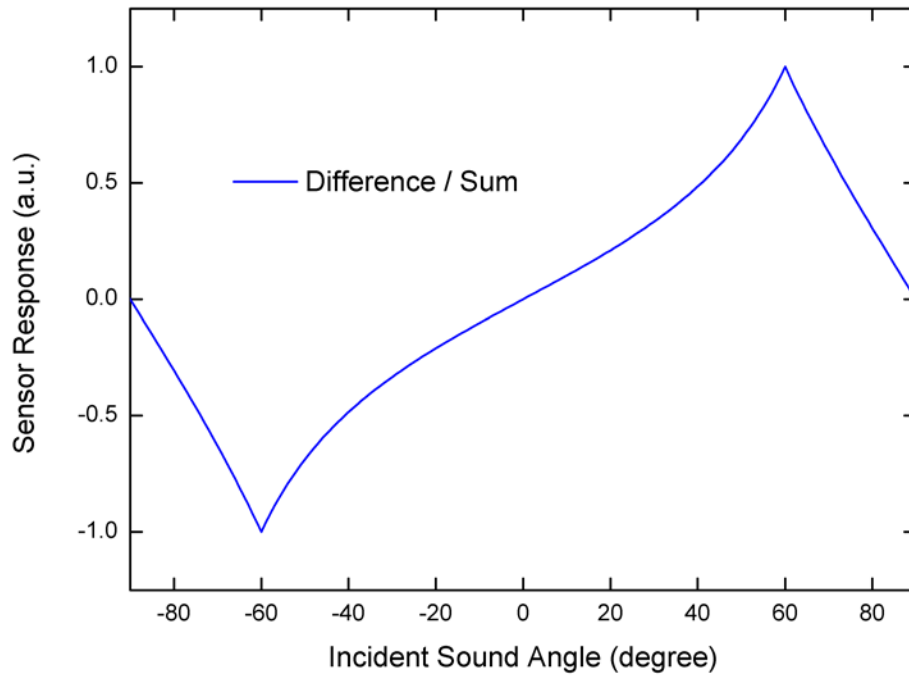
Matching the left side of (5) theoretical sensor output is plotted vs. incident sound angle.
Unambiguous readings cover the range of $\theta = \pm\, 60°$ from normal incidence, the effective
angular range of the sensor.

In practice, the dual sensor unit will be calibrated and the output normalized to balance any differences between individual sensors. The motivation and effectiveness of this approach are discussed in the next chapter.

III.   EXPERIMENTAL STUDY

A.   PRE-EXPERIMENT DEVELOPMENT

Prior to conducting the planned experiment a new sensor mount and circuit boards were designed and characterization of the latest generation of sensor carried out.

1.   Sensor Characterization

Figure 12 shows the latest generation of sensor used in experimental work for this thesis.

Figure 12   Generation 12 DF sensor.
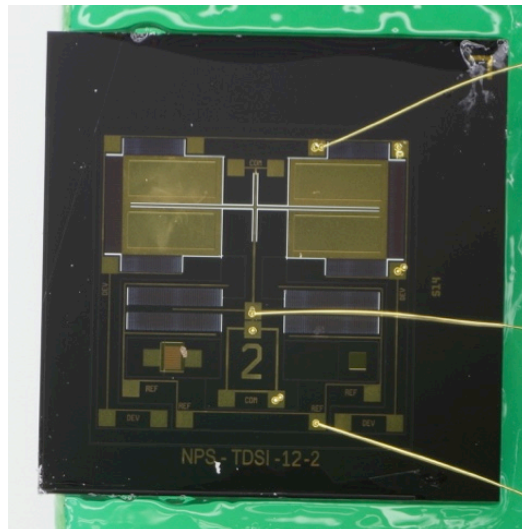
This generation 12 DF sensor is used for the experimental work in this thesis. The sensor is glued to the printed circuit board (PCB) with an open cavity below to allow for the acoustic pressure to interact with both sides of the device. The three wirebond connections provide the required capacitive inputs to readout circuitry.

Before experimental work could begin in the anechoic chamber, each individual sensor was excited with a linear sweep of sound to measure its frequency response. A laser beam from a laser vibrometer was shined on the outer edge of the sensor wing to measure wing displacement. The sound pressure level (SPL) at the sensor was found to

be approximately 54 dB. Table 1 details the settings of the laser vibrometer used to produce the frequency response in Figure 13.

Table 1   Laser vibrometer settings.

Setting	Value
Frequency Sweep	500-4000 Hz
Amplitude	0.1 A
Gain	5
Sweep Time	1.28 s
FFT Lines	12000

Figure 13   Frequency response of a single sensor.
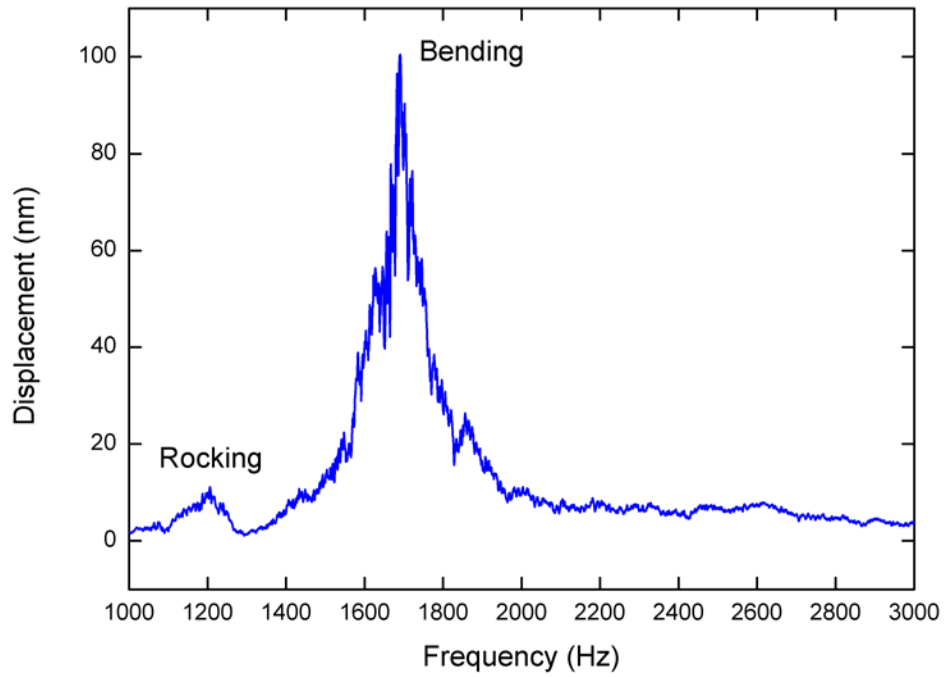
Rocking and bending resonant peaks are clearly seen in this data produced using laser
vibrometry.

The resonance frequency of the bending mode was confirmed as 1.690 kHz ± 20 Hz by laser vibrometry. At this frequency, the linear relationship between sound pressure and displacement was measured and is shown in Figure 14.

Figure 14   Displacement vs. sound pressure for a single sensor.
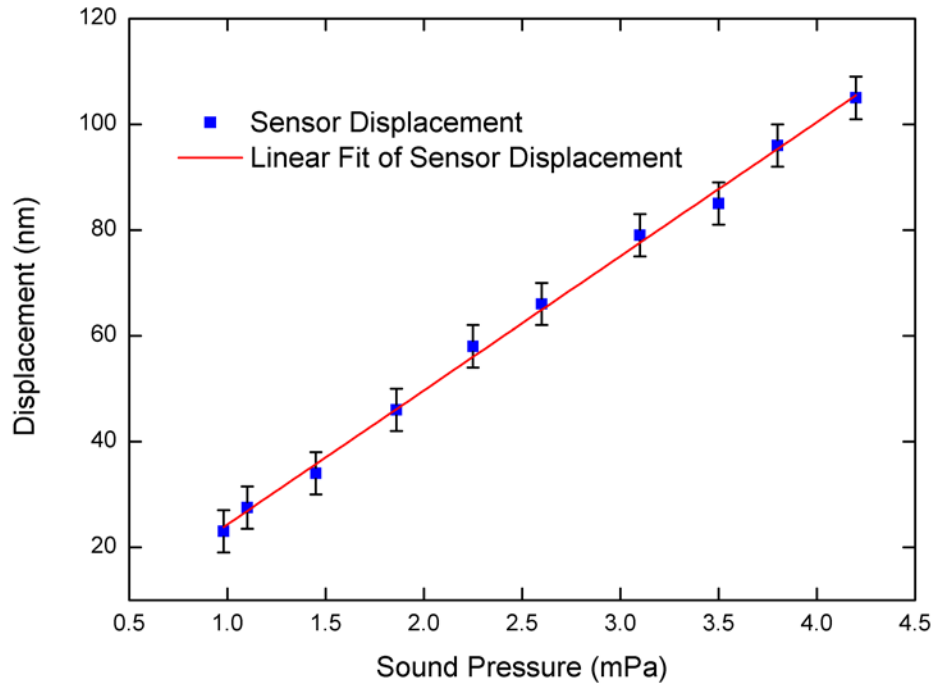
Sensor displacement using normally incident sound. Observed error using multiple measurements at each sound pressure was ±4 nm. The resulting sensitivity is 25 μm/Pa.

2.   Mount

In order to reliably form the dual sensor assembly at an angle θ_{off} (Figure 9), a mount was designed that uses nylon bolts to hold the sensors in position (Figure 15). The mount was printed on a MakerBot 3D printer and mounted atop a ½-in rod so it can be inserted into the anechoic chamber rotating chuck.

20

Figure 15   Mount design.
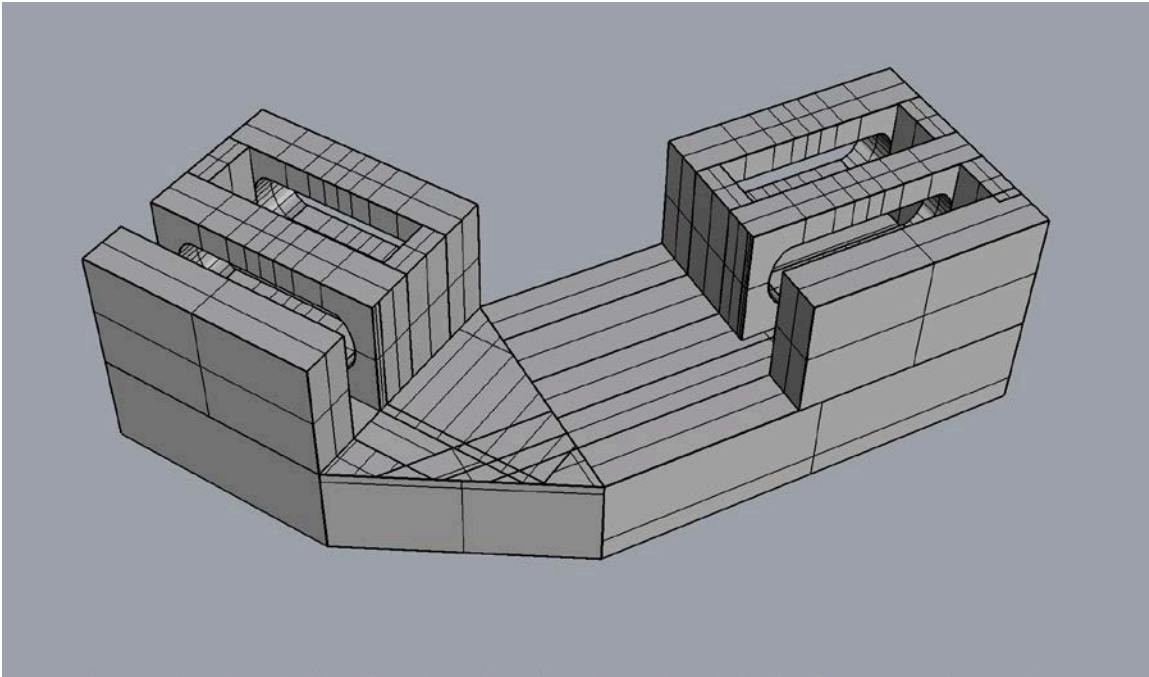
Design used to 3D print the mount that will hold both sensors at an angle of $\theta_{off} = 30°$ as per Figure 9. Nylon nuts and bolts are placed through the rear channels to provide a clamp to hold the PCBs.

3.   Printed Circuit Board

For electronic readout purposes, the Irvine Sensor Corporation MS3110 Universal Capacitive Readout IC is used. The MS3110 is a general purpose, ultra low noise complementary metal-oxide semiconductor integrated circuit CMOS IC intended to support a variety of MEMS sensors that require a high resolution capacitive readout interface [18]. This IC will translate the change in capacitance caused by movement of the sensor comb finger capacitors into an analog output. It is a 16-pin SOIC package that operates using 5V power supply supported by four stabilizing capacitors. Gain, bandwidth, and capacitive balancing are programmed using a PC-based utility to match the sensor and application required. All settings are stored in onboard electrically erasable programmable read only memory (EEPROM) that is automatically loaded when power is applied.

21

The previous generations of DF sensors were mounted with the MS3110 on a hybrid ceramic prototyping board. This approach was initially attempted, but it proved unreliable and time consuming to connect the sensor and readout electronics to the board using delicate wirebonding. In addition, this required that 12 individual wires be connected during the calibration and programming of the MS3110. While this allowed for flexibility during previous development projects, it was too cumbersome when working with co-located sensors, so a PCB was designed.

The PCB was designed using free layout software available from the fabrication facility used, Advanced Circuits [19]. A two-layer design is used, with copper interconnects and vias providing connections between elements on the top and bottom of the PCB. A solder mask is also applied to select areas to facilitate soldering the MS3110 chip, capacitors, switches, voltage regulator, and connectors. Finally, bondable gold is added to three connection pads allowing for the sensor to be linked to readout circuitry using wirebonding techniques.

The PCB has the following important features:

1.   Interconnections to minimize the number of wirebonds required during construction

2.   A robust wire connection to the MS3110 programming board

3.   Battery power source

4.   On/off power switch

The circuit schematic is shown in Figure 16, and the PCB layout is shown in Figure 17.

Figure 16   Circuit schematic.
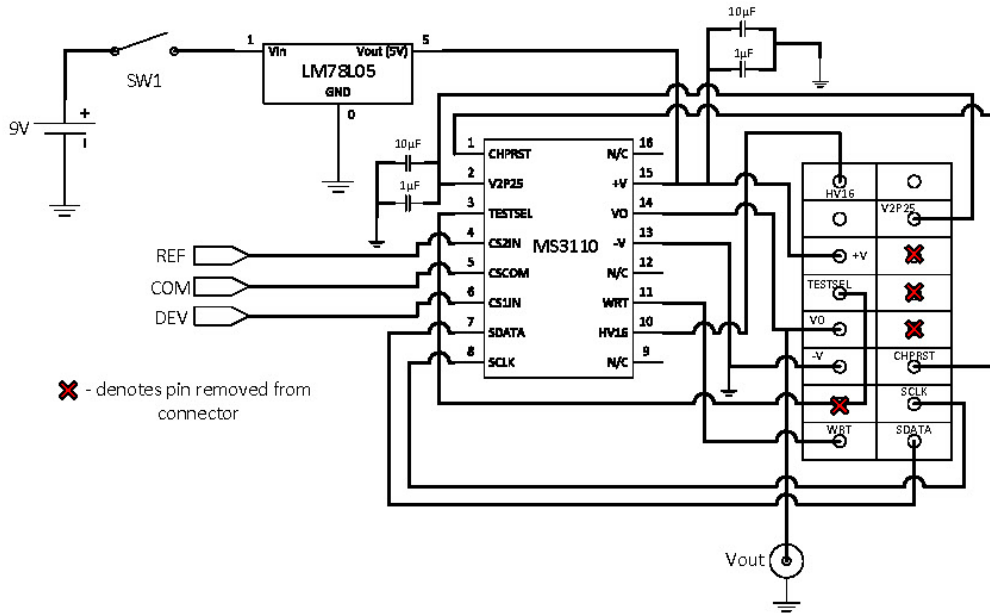
The circuit schematic of the PCB details all components required to support the sensor. The 9V source shown is a standard battery, in this case an Energizer 522, which supplies a LM7805 voltage regulator, which in turn powers the circuit at 5V. The MS3110 interfaces the sensor (COM, REF, and DEV connections) with programming pins and V_{out} on the right side of the schematic. COM provides a common reference between the sensor and IC. REF and DEV connect to either side of the comb finger capacitors, allowing differential measurement to take place.

Figure 17   PCB layout.
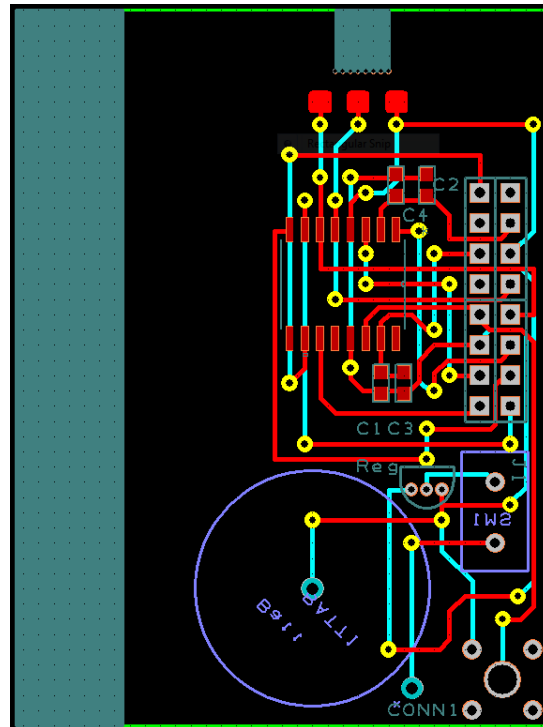
The PCB is a two-layer board measuring 1¾ by 2¼ inches. Purple and teal items are silkscreened reference markers. The large area on the left allows for clamping and can be removed after fabrication. The square at the top is bordered by small holes and gets removed to allow for a cavity below the MEMS sensor. Routes and vias form a copper layer with solder masking on the red pads shown. Bondable gold is also added to the top surface to permit wirebonding between the sensor and three adjacent connection pads.

a.   Battery Power

As can be seen in Figure 17, the PCB is designed to use a coin cell battery holder. The intention was to use two 3V Panasonic CR1612 batteries in series to provide 6V to operate the board at 5V via a LM78L05 voltage regulator. These batteries proved to have insufficient capacity, offering only 40 mAh to the circuit [20]. The MS3110 readout chip is rated to draw between 3 and 6 mA [21]. This meant that the batteries drained too quickly for practical use in testing or operation.

The solution was to use an Energizer 9V battery with a capacity of 400-600 mAh [22], located externally.

24

b. *Output Wires*

The intent for connecting the output signal was to use a SubMiniature version A (SMA) connection at the bottom right corner of Figure 17. The connectors ordered unfortunately did not match the holes in the PCB design, so individual wires were soldered to the connections in a twisted pair configuration.

c. *Connection to Programming Board*

A 16-wire flat ribbon cable was used to connect the PCB to the MS3110 programming board. The programming board was originally designed to program and calibrate the MS3110 chip before it is soldered onto a PCB. Modifications were made so the MS3110 can be programmed at any time. The programming board, detailed in [18], has a 16-pin connection (J10) that provides some of the output required; the remaining connections were made with wire on the underside of the board. The board is well marked, and there are numerous soldering points to connect the required points on the board (HV16, V2P25, +V, Vout, and J9A) to J10. The pinout of J10 is shown in Figure 19. These modifications ensure that the MS3110 programming board will program the chip after the PCB is assembled, a vital capability to balance the capacitance and output gain of the sensor.

Figure 18 shows a photo of the top of the programming board. Figure 19 details a basic schematic of the board and the changes made to jumper J10 to use it as a ribbon cable connection with the sensor. Figure 20 shows the underside of the programming board to highlight the wire connections made to J10.

Figure 18　MS3110 programming board.
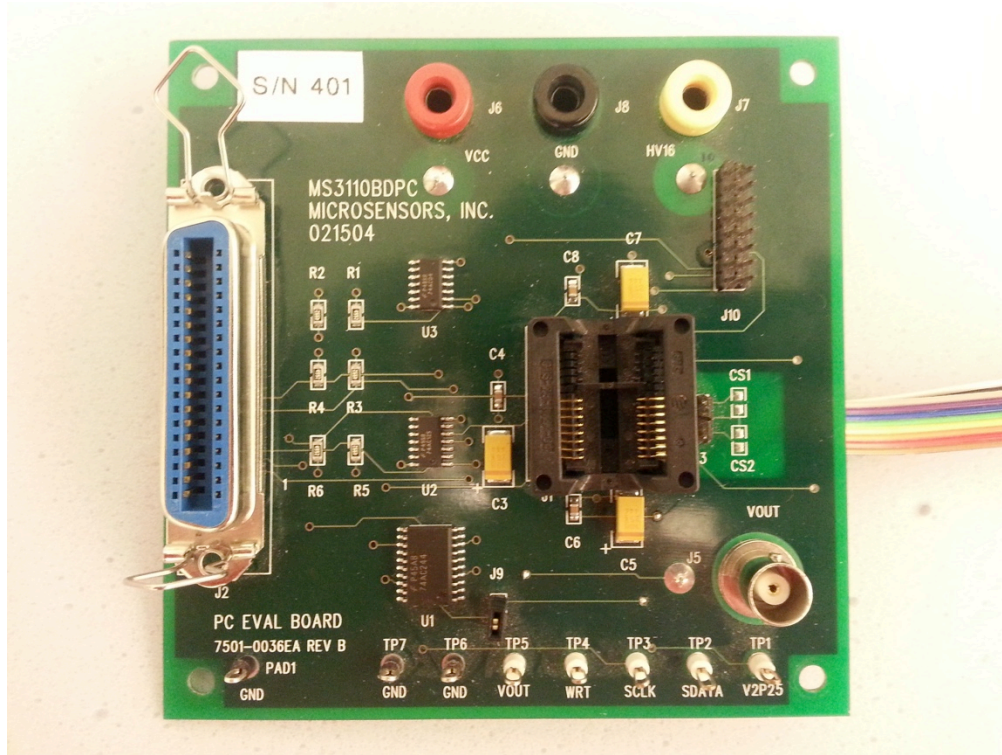
This board is used for sensor setup that is essential for the sensor output to operate in the desired gain and sensitivity ranges.

Figure 19   Programming board schematic.
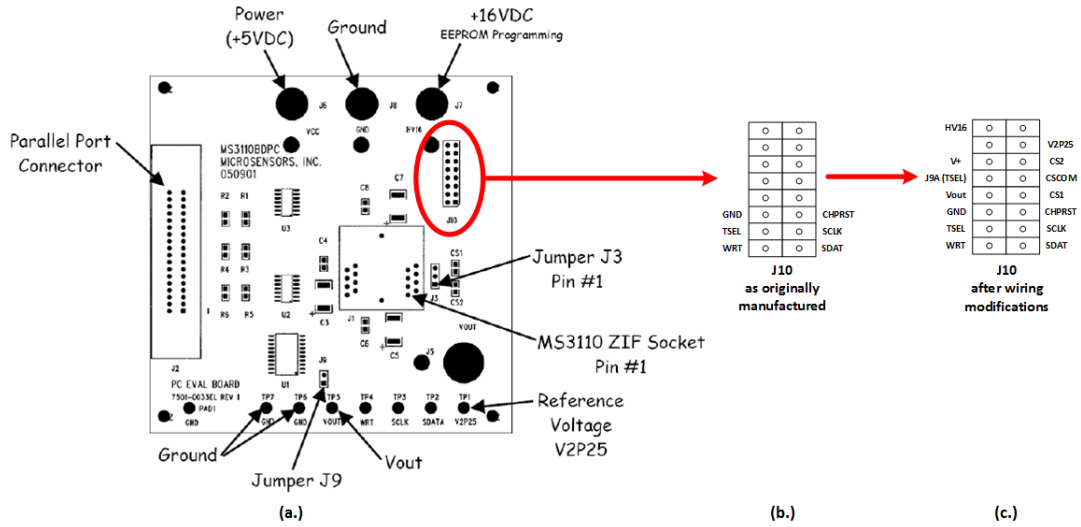
(a.) Programming board schematic from the original manufacturer. (b.) Original J10 connections hard wired in the programming board by the manufacturer. (c.) Completed J10 pinout achieved by soldering new wires on the underside of the programming board. These connections match with the sensor PCB via ribbon cable to permit programming of the sensor at any time.

Figure 20   Programming board bottom view.
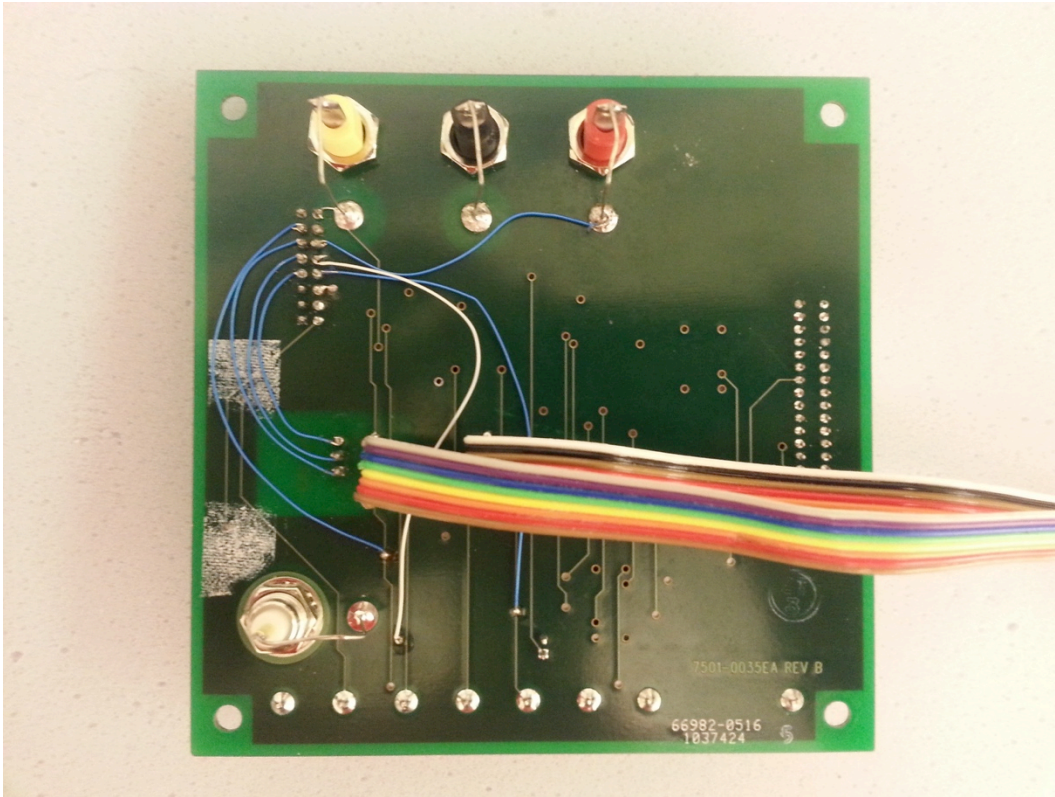
This view shows additional wires used to set up programming connection using J10. Each connection has multiple possible sources on the programming board and can come from any point on the board. The only exception to this is the J9 TESTSEL line, which must be taken from the bottom pin of J9. The ribbon cables shown here are not used and remain only to provide legacy support to previous generation sensors.

d.   *Bondable Gold*

To make the PCB bond pads receptive to wirebonding, gold must be laid over the three connection pads seen in Figure 17. The simplest way of doing this during manufacturing is to have soft bondable gold laid over all of the copper wire on the board, including the connection pads. To improve bonding thicker gold is generally better [23]. For this project. a minimum of 20 microinches of soft bondable gold was added during manufacturing.

Once modifications were made to the programming board, the PCB sensor assemblies were constructed using PCB soldering techniques and three wirebonds between the sensor and connection pads using a Leica 4524A Digital Wirebonder (Figure 21). The delicate wirebonds were done last using careful placement of the PCB to avoid heat damage to any components (Figure 22). The wirebonder settings used are shown in Table 2.

Figure 21   Leica 4524A Digital Wirebonder.

Figure 22   PCB on Leica 4524A Digital Wirebonder heat table.
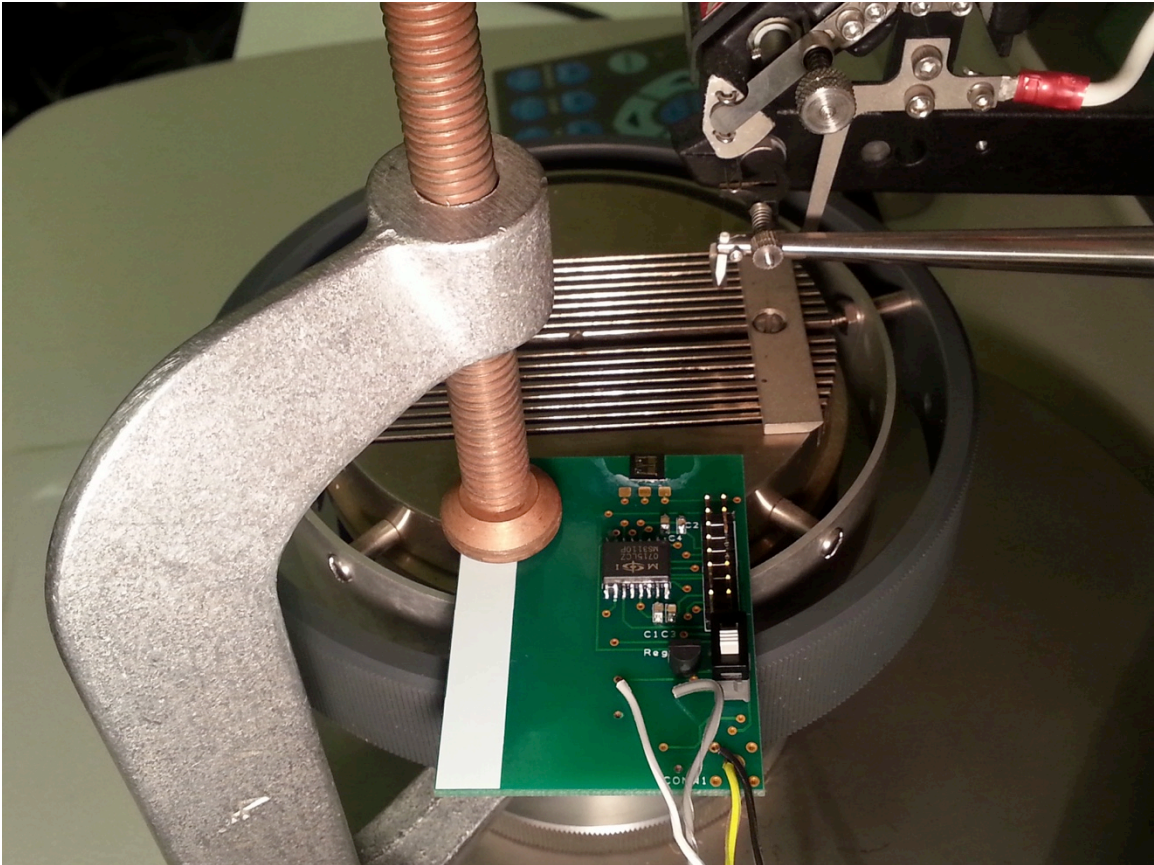
The PCB is held on Leica 4524A Digital Wirebonder heat table with a C
clamp. This allows heat to be applied to the PCB underneath the sensor
and three connection pads while protecting the readout circuitry.

Table 2   Wirebonding settings.

	First bond (Sensor)	Second Bond (PCB)
Search	1.2	1.2
Power	1.8	1.6
Time	5	7
Force	1.2	3
Loop	-	5
Tail	-	4
Ball	-	3.5

The most difficult bond is the second bond onto the PCB connection pads. Just prior to bonding, the pads are cleaned with isopropanol to remove residue and oxidation. The time, force, and tail settings were frequently adjusted to successfully complete the second bond.

Two modifications need to be made to the PCB before it will function correctly. Due to oversight in the design, PCB pins PCB4 and PCB7 need to be connected with a wire. This is due to confusion of the nature of the test select (TESTSEL) line on the programming board during design. During normal operation, jumper J9 makes the TESTSEL line continuous. When calibrating the sensor in accordance with [24], one step requires J9 to be removed and the current in the line adjusted to 10 μA. For this reason the PCB must be connected to the correct (bottom) side the TESTSEL line when it is split by J9, an issue solved by connecting pins PCB4 and PCB7 on the bottom of the PCB and removing the top connector portion of PCB7.

Shown in Figure 23, pins PCB12, PCB13, and PCB14 must be removed to isolate the CS1, CS2, and CSCOM connections. These are the three connections that the MS3110 uses to measure the change in capacitance as sensor wings move, so they must be as short as possible with no extraneous connections.

Figure 23   PCB ribbon cable connection.

PCB Ribbon cable connection

X - denotes pin removed from connector
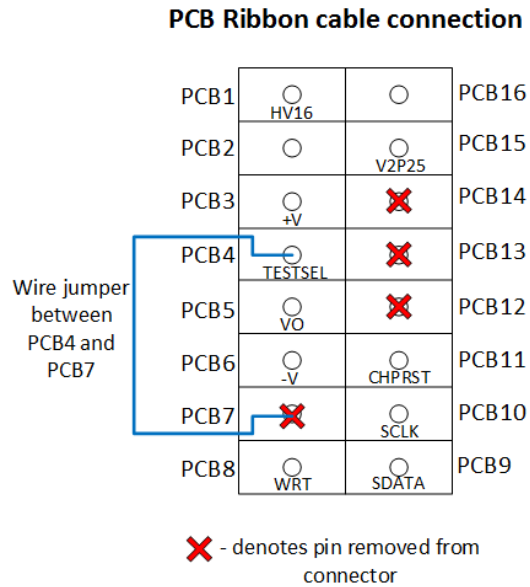
Details of the PCB ribbon cable connection. One jumper wire is required and should be soldered on the underside of the board. Pins with an 'x' should be removed with wire cutters such that they do not make connection with the ribbon cable.

This preparation work resulted in two PCB-based sensors (Figure 24) mounted for experimental work (Figure 25).

Figure 24   Assembled PCB.
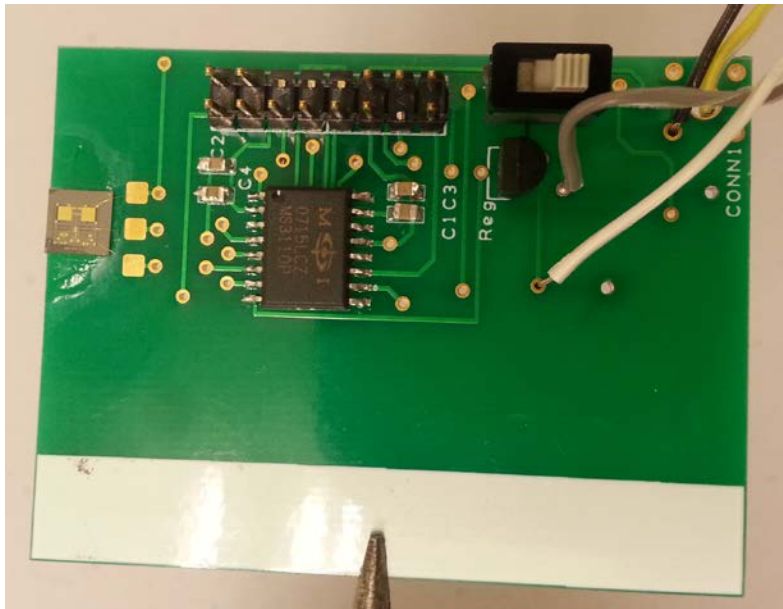
A fully assembled PCB with sensor and readout circuitry. The sensor on the left is glued to the PCB with a cavity underneath to allow for interaction with both sides of the sensor wings. The MS3110 capacitive readout is centrally located with four stabilizing capacitors (C1 through C4). At the top of the board is the ribbon cable connection used for programming and a power switch to conserve battery life. The 5V regulator (Reg) supplies power from the external 9V battery via the power switch. Output is taken from the top right corner (CONN1).

Figure 25   Dual sensor assembly.
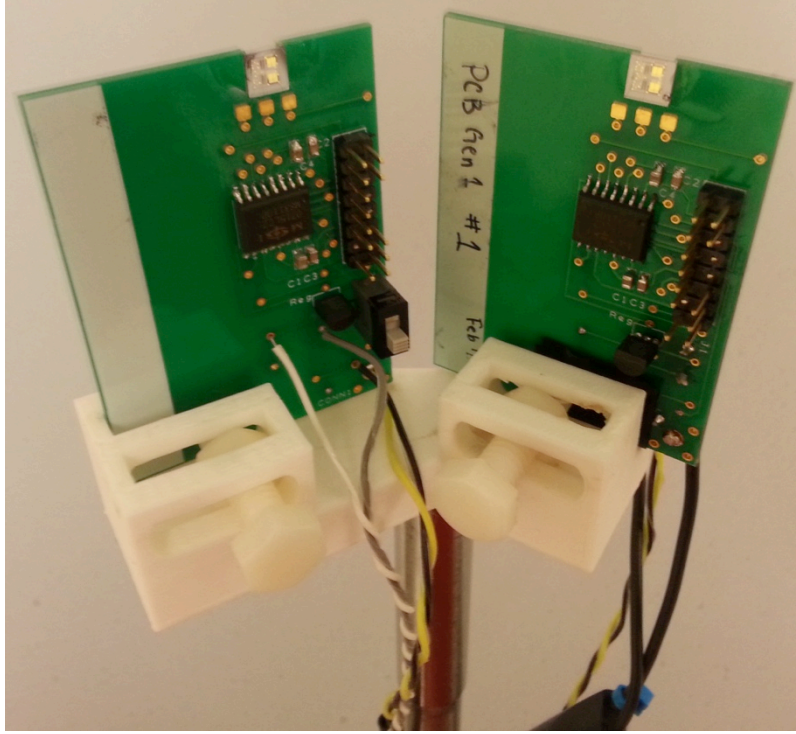
Dual sensor assembly as operated. Both sensor PCBs are identical and mounted at $\theta_{off} = 30°$. One external 9V battery (not shown) powers both sensors.

4.   Sensor Capacitance Balancing and Gain Setting

As detailed in [18], in order for the MS3110 to properly react to changes in capacitance at the sensor, it must be balanced using the built-in internal capacitors. The desired gain is set according to the expected capacitance variations and intended sound level. This gain affects the output, V_o, according to the MS3110 transfer function:

$$V_o = V_{ref}(1.14)(GAINSEL)\left(\frac{CS_2 - CS_1}{CF}\right) + V_{ref} \tag{7}$$

where V_{ref} is the MS3110 reference voltage, GAINSEL is the output buffer gain selection, CS_2 and CS_1 are balance trim capacitors, and CF is the feedback capacitor. The procedure in the MS3110 Quick Start Guide explains how to set the values of CS_2, CS_1 and CF [24]. For this project, V_{ref} is set to 2.25 V and GAINSEL set to 4.

If internal gain is set too low, then nothing will be detected. Conversely, set the gain too high and the chip output will saturate, rendering a constant output. Prior to the final experiment, measurements were made to determine the lowest source level that a single sensor could detect. Table 3 shows the settings used for these high gain measurements.

Table 3   MS3110 high gain settings used to determine the highest voltage to displacement performance offered by the sensor.

CF	0.513 pF
CS1	0.437 pF
CS2	1.197 pF
Gain	4
LPF 3dB Frequency	3.0 kHz

The sensor response at different sound levels was verified to ensure it replicated previous results in [15]. The sensor responded as expected down to a sound level of 33dB (Figure 26). Below this level, the sensor continued to respond with a similar cosine shape but was significantly degraded by noise within the testing chamber.

The experimental setup to obtain the data shown in Figure 26 is explained in detail in Chapter III.B.

Figure 26   Single sensor response at varying sound levels.
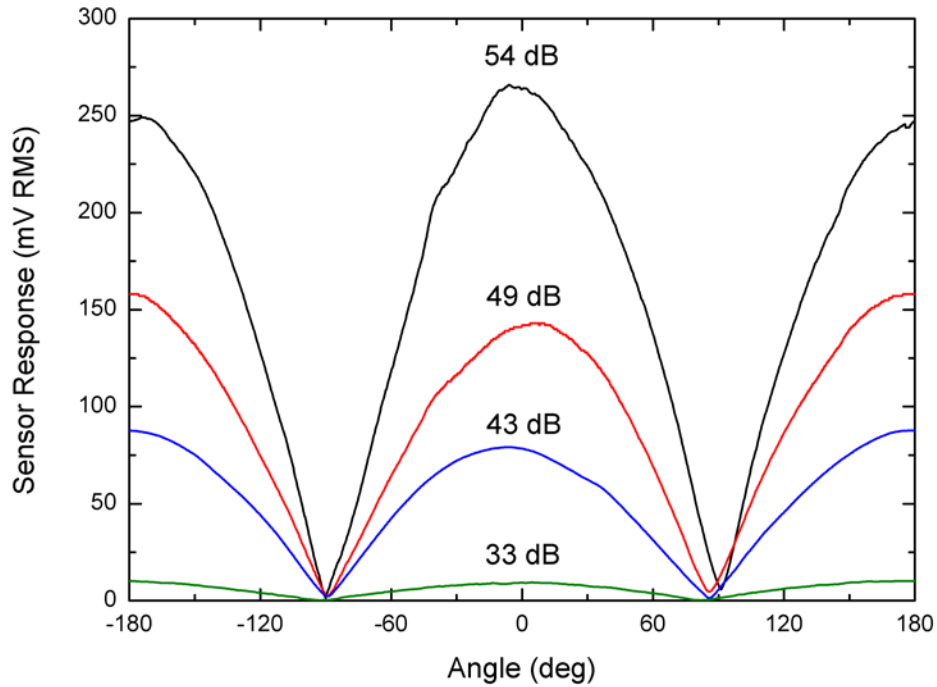
360° sweeps of a single sensor using high gain settings found in Table 3.

For DF measurements using two sensors, the settings in Table 4 were used.

Table 4   MS3110 normal operation settings used for DF operations.

	Sensor 1	Sensor 2
CF	0.988 pF	0.513 pF
CS1	0.114 pF	0.437 pF
CS2	0.171 pF	1.197 pF
Gain	4	4
LPF 3dB Frequency	3.0 kHz	3.0 kHz

The sensitivity of an individual sensor was tested and plotted as voltage output vs. incident sound pressure at the sensor. Pressures varying from 1 to 4 mPa at normal ($\theta = 0°$) were used to show that the sensor response is linear. With the gain settings of

Sensor 2 in Table 4 the sensitivity is calculated to be 260 V/Pa (Figure 27), which corresponds to 0.1 V/nm (displacement of the wing edge).

Figure 27   Sensor sensitivity.
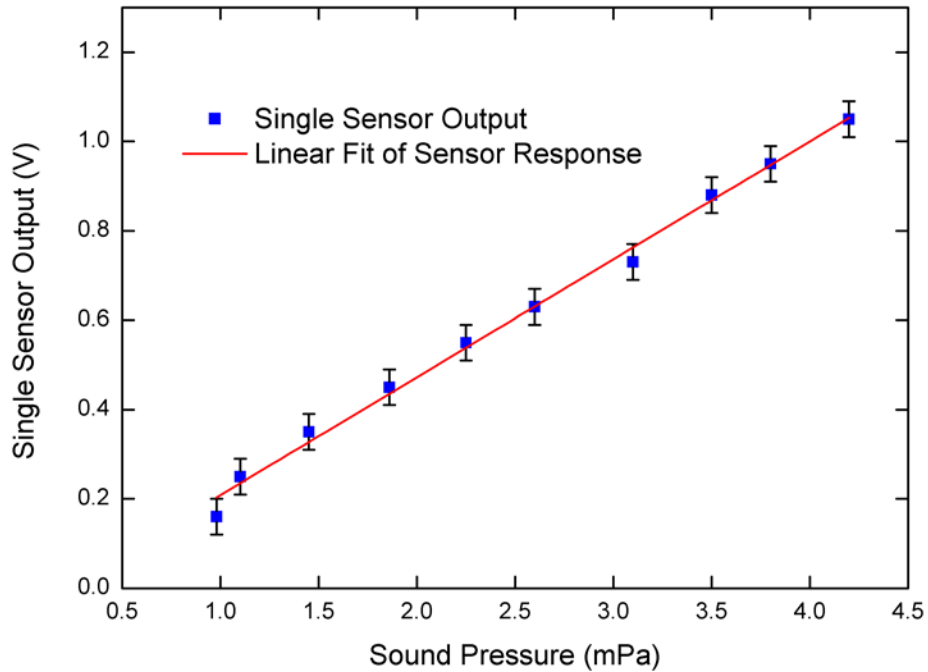
Single sensor output using incident sound at $\theta = 0°$. Variations in measurements gave the output an error of ± 0.04 V. The resulting sensitivity of a single sensor is calculated as 260 V/Pa using a linear fit line.

B.   EXPERIMENT SETUP

After the pre-experiment development was completed, the NPS anechoic chamber was set up to perform a DF experiment using the dual sensor assembly shown in Figure 25. This section describes the equipment and configuration used to conduct this experiment as shown in Figure 28.

Figure 28   Experimental setup diagram.
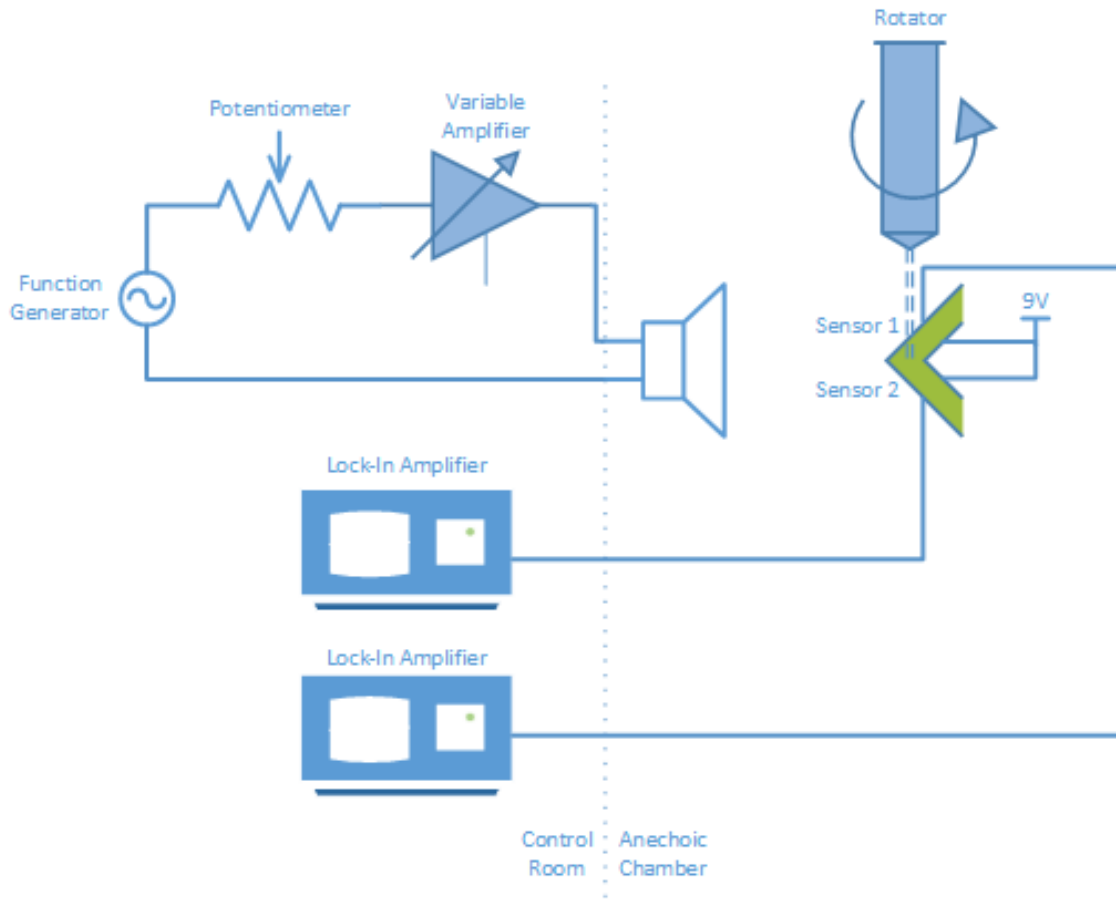
Experimental setup in the NPS anechoic chamber and control room. The sensor assembly
is mounted on a remote controlled rotator 5 m away from the speaker used for excitation.
This speaker is driven by a function generator, potentiometer, and variable amplifier to
achieve the desired sound level at the sensor. Lock-in amplifiers, one per sensor channel,
are used to capture the sensor output.

1.   Excitation

The excitation used for the experiment is a sine wave at 1690 Hz of varying
amplitude. This frequency is sufficiently near the resonance frequency of both sensors to
generate a strong response (Figure 29). A typical gunshot creates broadband sound over
125 to 5000 Hz [25], and the excitation frequency is suitable for detecting a gunshot.

Figure 29   Frequency response of sensors.
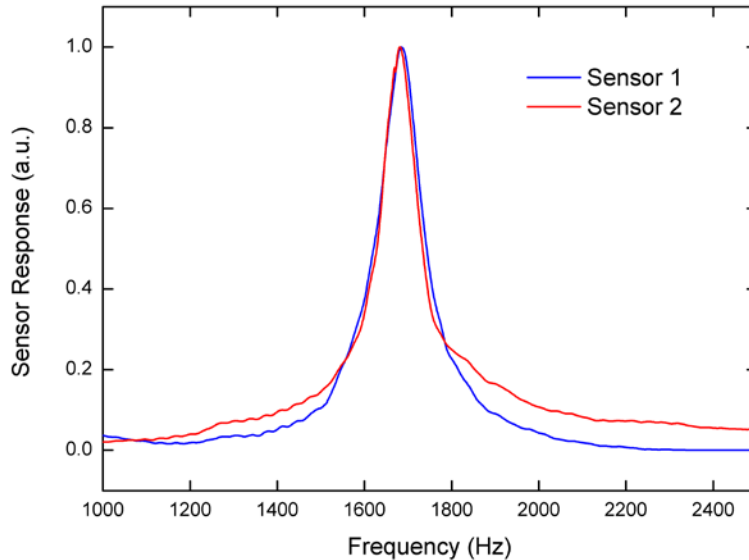
A speaker located at normal incidence to each sensor ($\theta = 0°$) provided a frequency sweep to measure the frequency response of both sensors. Both sensors are from the same fabrication lot and demonstrate a similar resonant frequency of approximately 1690 Hz.

The 1690 Hz signal is created by an Agilent 33220A signal generator. This generator uses a digital to analog converter to create the signal. To ensure that the generator functions in a region that noise and quantization errors are minimized two further elements are included: a variable amplifier and potentiometer. The amplifier allows for the SPL to be raised with gain of 1, 2, 5, and 10. The potentiometer is used to reduce the SPL without changing the function generator amplitude, thus keeping the function generator at an optimal output level. The potentiometer forms a voltage divider with the speaker, effectively reducing the voltage (amplitude) driving the speaker.

To calibrate this signal generation circuit, a B&K pressure field microphone is placed as close as possible to the dual sensor assembly position and readings taken using the arrangement shown in Figure 30.

Figure 30   Source calibration using omni-directional microphone.
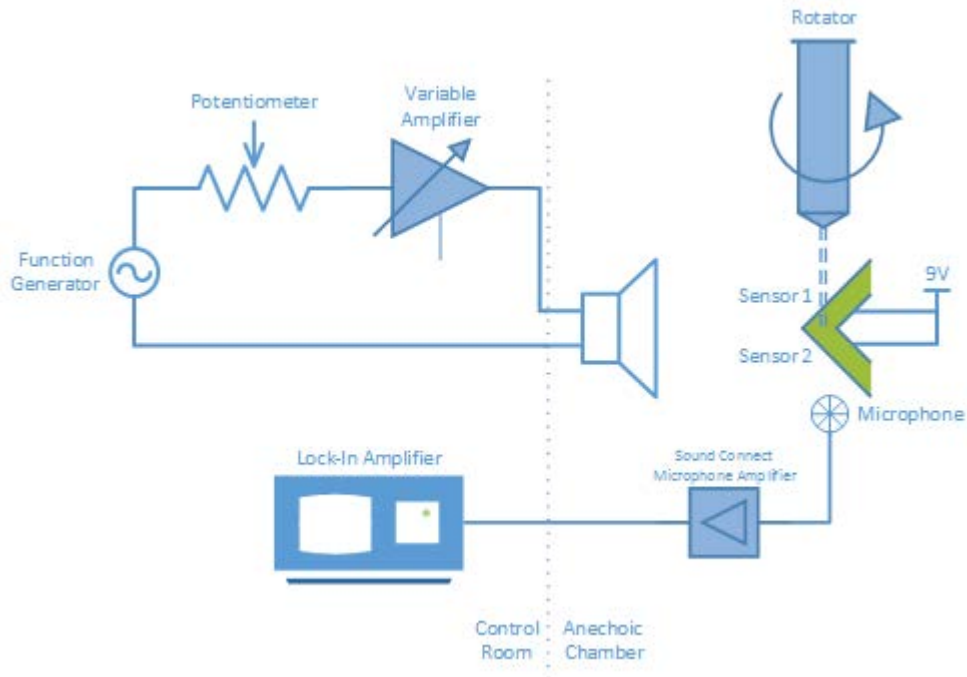
Setup for sound source calibration using a B&K pressure field microphone. Taking
readings in the optimal operating region of the microphone (over 52 dB) allows a
calibration graph to be created. This calibration graph is used to predict the sound level at
the sensor as the amplitude is lowered. Although not required for actual direction finding,
the sound level used shows sensor performance.

The omnidirectional microphone's optimal operating region is above 52 dB, so a
series of readings were taken to generate a linear best-fit line [26]. The output of the
B&K microphone is amplified by an inline amplifier and captured using a Stanford
Research Systems SR850 Lock-In Amplifier. The resulting calibration graph is shown in
Figure 31 and equations (8) and (9). The outputs of the signal generator, amplifier, and
potentiometer are linear, giving a linear relationship between the function generator
output and SPL.

Figure 31   Omni-directional microphone calibration results.
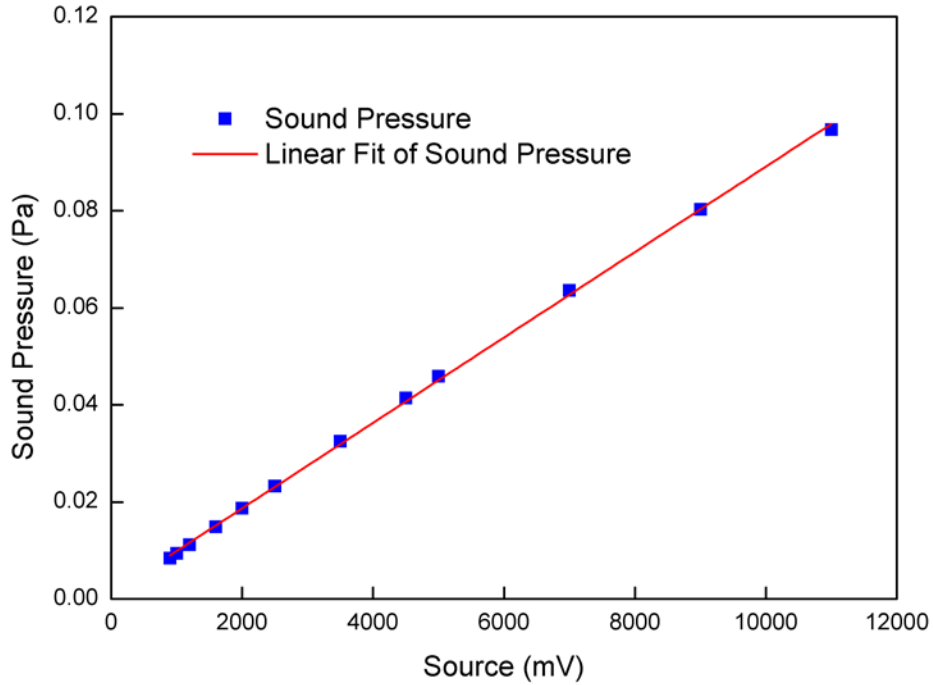
To gain accurate knowledge of the sound level at the sensor an omni-directional microphone was used to calibrate the speaker and driver used. Operating the microphone above the minimum manufacturer prescribed sound pressure level, measurements were taken and a linear fit line produced using the source excitation voltage as independent variable. Observed variations in lock-in amplifier output and microphone specifications gave an error of 0.002 Pa to the measurements. This approach allowed accurate prediction of the sound level at the sensor using sound levels below the minimum threshold of the microphone.

$$Sound\ Pressure\ [Pa] = 0.0011 + (8.8028 \times 10^{-6}) * source\ [mV] \qquad (8)$$

$$SPL = 20 * \log\left(\frac{Sound\ Pressure\ [Pa]}{20[\mu Pa]}\right) re\ 20\mu Pa \qquad (9)$$

2.   Sensor Normalization and Reference Curve

To compensate for individual sensor characteristics due to fabrication and assembly differences, a reference curve is generated before the dual sensor assembly can provide DF information. This allows for the output from each side of the sensor to be

41

normalized between 0 and 1, removing any variations between individual MS3110 outputs due to the nature of balancing capacitance and gain (as discussed in Chapter III.A.4).

The theory provided in Chapter II can be adapted to allow for this normalization

$$\alpha_1 P_L = \alpha_1 P_o \cos(\theta - \theta_{off}) = P_n \cos(\theta - \theta_{off}) \tag{10}$$

$$\alpha_2 P_R = \alpha_2 P_o \cos(\theta + \theta_{off}) = P_n \cos(\theta + \theta_{off}) \tag{11}$$

where α_1 and α_2 are normalization constants adjusted such that $\alpha_1 \cdot \max(P_L) = 1$ and $\alpha_2 \cdot \max(P_R) = 1$, therefore the normalized magnitude, $P_n = 1$.

Combining the difference and sum of both returns allows for cancellation of the source level and resolution of angle ambiguity.

$$\frac{P_L - P_R}{P_L + P_R} =$$

$$\frac{P_n \cos(\theta - \theta_{off}) - P_n \cos(\theta + \theta_{off})}{P_n \cos(\theta - \theta_{off}) + P_n \cos(\theta + \theta_{off})} \tag{12}$$

$$\frac{P_n}{P_n} \left(\frac{\cos(\theta - \theta_{off}) - \cos(\theta + \theta_{off})}{\cos(\theta - \theta_{off}) + \cos(\theta + \theta_{off})} \right)$$

The use of common trigonometric identities simplifies this to:

$$\frac{\alpha_1 P_L - \alpha_2 P_R}{\alpha_1 P_L + \alpha_2 P_R} = \tan(\theta_{off}) \tan(\theta) \tag{13}$$

which can be readily solved in terms of the known quantities of a received sound:

$$\theta = \tan^{-1} \left(\frac{1}{\tan(\theta_{off})} \frac{\alpha_1 P_L - \alpha_2 P_R}{\alpha_1 P_L + \alpha_2 P_R} \right), \; -60^{\circ} \leq \theta \leq 60^{\circ} \tag{14}$$

The normalized experimental data for the two sensors as a function of direction of sound are shown in Figure 32. Both sensors show slight offset from the expected locations of the null responses, which could be due to the interaction of sound with the relatively large package used in the measurement.

42

Figure 32   Measured normalized response of left and right sensors.
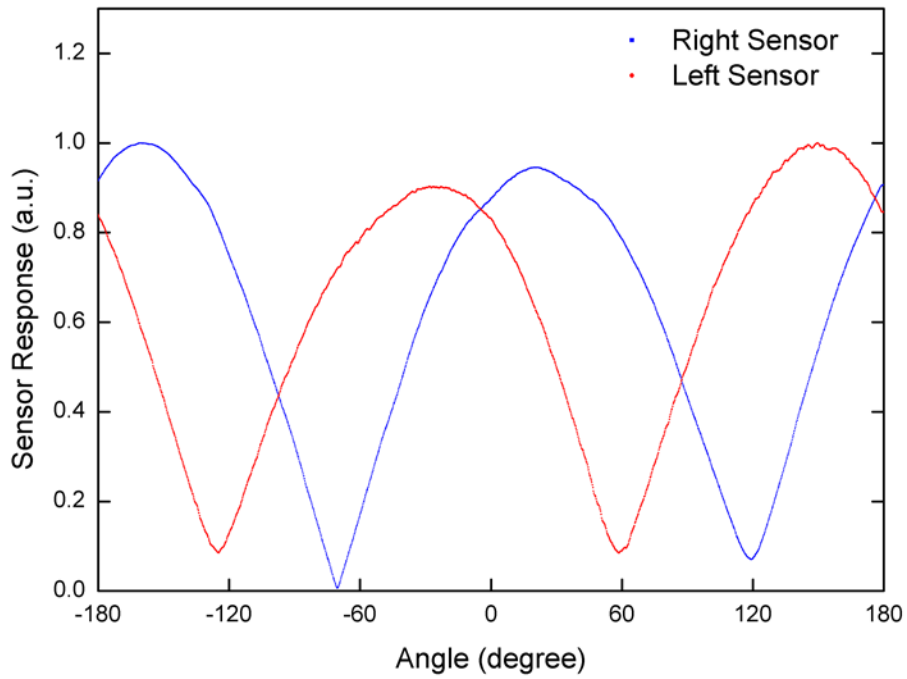
Sensor responses were normalized using $\alpha_1 = 9.7898$ and $\alpha_2 = 30.187$ as per (10) and (11).

Subsequent DF measurements will use $\alpha_1 = 9.7898$ and $\alpha_2 = 30.187$ and (14) to determine the direction of incoming sound.

THIS PAGE INTENTIONALLY LEFT BLANK

IV. MEASUREMENTS AND RESULTS

To demonstrate that the knowledge of the sound source level of an incoming signal is not required when taking DF measurements, the dual sensor assembly was placed at known angles while varying the level of incident sound.

To cancel out the unknown sound level of the source, the experimental responses of the left and right sensors in Figure 32 were combined, taking the ratio of their difference and sum as described in Chapter II Section 2. The result is shown in Figure 33.

Figure 33   Difference of sensor signals divided by their sum.
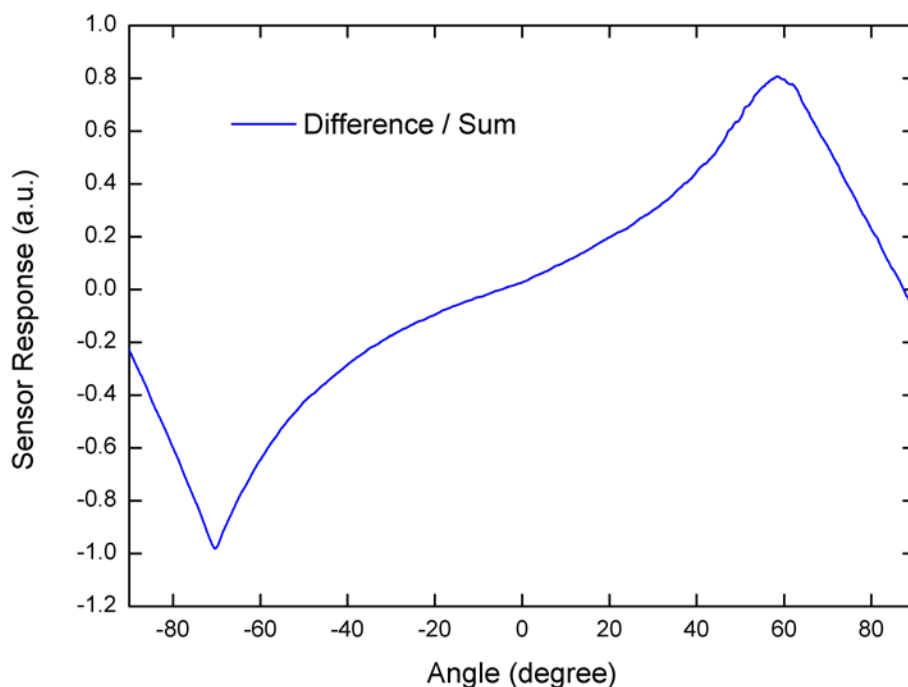
Plot of individual sensor output difference divided by sum as in (13). This plot follows that expected by theory with the only notable offset at $\theta = -60°$. This offset does not impede the sensor from direction finding over the intended angular range of 120°.

Figure 33 shows good agreement to the theoretical predictions shown in Figure 11. The intended range of $\theta = \pm60°$ is successfully covered with no ambiguity and can be

used for direction finding. Notable departures from theory occur at the extremes of the angular range, ±60°. At these large angles, the sensor response does not reach the theoretical values of ±1. The source of this can be due to the offsets observed in Figure 32, where the amplitude of both sensors does not fully reach 1 a.u. and nulls do not go to 0 exactly at their respective minimums. This is the result of individual sensor output that follows, but does not exactly replicate a cosine shape in (1). As mentioned earlier, this could be due to reflections of sound from components around the sensor such as the PCB, mount, and wires. The effect of these deviations is minimized by normalizing the magnitude of individual sensor outputs and does not inhibit the sensor's ability to find direction.

The outputs of the sensor were measured for a set of angles between +/- 60° with varying sound pressure from 33 to 54 dB. Then the outputs were processed (as detailed in Chapter III.B.2) to obtain the angle, and the results are shown in Table 5, where SPL is the measured sound pressure level at the sensor. For each angle of incidence, average of the measured direction over the source level and its standard deviation (S.D.) are also shown in Table 5.

Table 5   Measured angles at 10° increments of incident direction.

Angle (°)	Sensor Result (°)						Average Measured Angle	Average Deviation	S.D.
	SPL (dB)								
	33	35	37.5	42	49	54			
-60	-58.75	-55.00	-56.50	-56.25	-57.00	-58.50	-57.0	3.0	1.30
-50	-50.75	-51.25	-53.75	-53.75	-54.00	-51.50	-52.5	2.5	1.35
-40	-40.25	-42.25	-41.50	-42.50	-43.50	-40.25	-41.8	1.8	1.19
-30	-31.00	-30.25	-31.25	-32.5	-31.75	-30.75	-31.2	1.2	0.72
-20	-20.75	-24.00	-21.25	-22.5	-24.25	-18.75	-21.9	1.9	1.91
-10	-11.00	-10.00	-7.50	-10.00	-9.50	-10.75	-9.8	0.2	1.14
0	-2.00	-1.75	1.75	0.50	-0.25	-0.25	-0.3	0.3	1.28
10	10.00	9.25	9.75	9.75	11.25	11.00	10.2	0.2	0.72
20	19.50	15.75	18.75	19.50	16.00	21.00	18.4	1.6	1.92
30	28.50	29.25	29.25	28.50	27.00	30.5	28.8	1.2	1.06
40	38.00	38.50	37.50	36.50	36.50	39.75	37.8	2.2	1.14
50	47.50	47.00	46.00	46.00	46.00	47.75	46.7	3.3	0.74
60	59.00	54.50	56.25	56.25	54.75	59.00	56.6	3.4	1.81

The average sensor result across all sound levels measured, along with an ideal theoretical reference line are plotted in Figure 34. The source levels used (33 to 54 dB) lie in the normal operation range of the sensor where the response is linear (no saturation of the sensor output occurred). The data shown confirms that the sensor can accurately determine the direction without knowing the source strength.

Figure 34   Measured angle results for sound pressure between 33 and 54 dB.
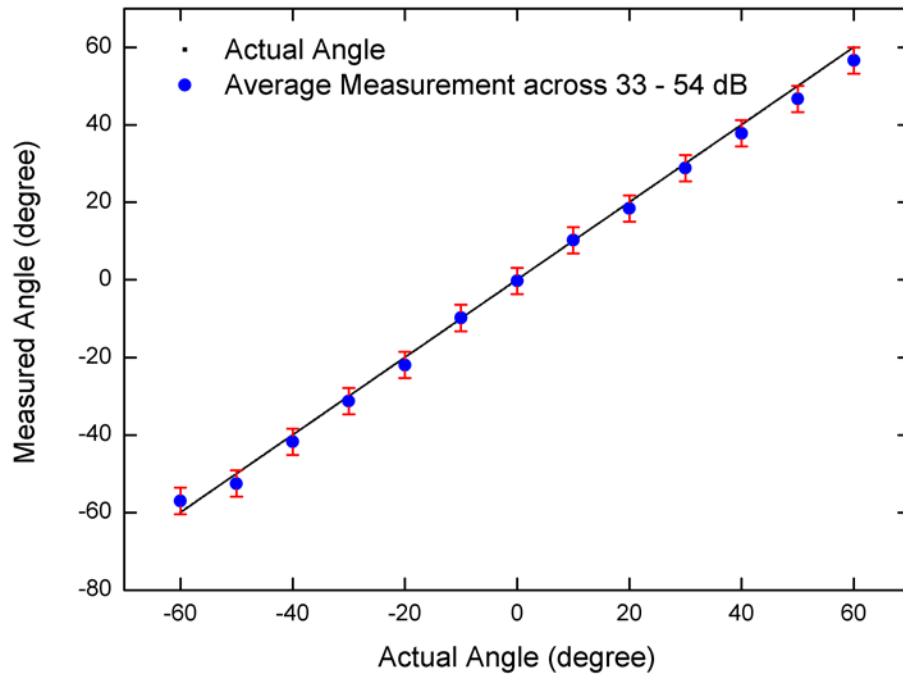
Experimental results plotted using the average sensor result information in Table 5. Six measurements were averaged over sound levels varying between 33 and 54 dB to create each data point. Sound level had no effect on the sensor's ability to direction find the source at these levels.

Errors in the measurements taken were consistent across all sound levels, so a varying sound level does not introduce errors when in the operating range of the sensor. Across the range of angles measured, the greatest errors were found on the outer angles of the measurement range, near ± 60°. This gave a maximum error of 3.4° with a standard deviation of 1.8°. These deviations were mainly due to spurious reflections off other parts of the sensor assembly and equipment in the anechoic chamber. This caused individual sensor outputs to vary from the expected cosine shape in (1) and resulted in minimums and maximums that do not reach 0 and 1 (see Figure 32). These variations introduced error that grew larger as the relative angle increased. Smaller systematic errors at all angles are attributed to noise in the readout circuitry and coaxial connection between the chamber and control room.

Considering these sources of error, Table 5 lists the average sensor result across all sound levels, along with the average error and standard deviation of the readings taken. Figure 34 plots the average angle across all sound levels in 10° increments using the maximum error observed, 3.4°.

THIS PAGE INTENTIONALLY LEFT BLANK

V. CONCLUSION

A. SUMMARY

A MEMS direction-finding sensor has been developed similar to the mechanically coupled ears of the *Ormia ochracea* fly. The mechanical coupling of the ears gives two resonant frequencies for the rocking and bending modes that allow for precise angle of arrival calculation. While in nature the fly is suspected of using both modes, the MEMS sensor developed capitalizes on the bending mode. This mode is strongest for sources that are normal to the sensor where the pressure differential between the front and back surfaces is largest. At the beginning of this study, a single sensor had been paired with an Irvine Systems MS3110 readout chip. The resulting output followed a cosine dependence with a peak output at normal incidence diminishing to minimum output at $\pm$ 90° similar to a pressure gradient microphone.

This was an important success in the development of an acoustic direction-finding system, but there remained important limitations that needed to be overcome. The sound pressure level at the sensor had to be known to determine the angle of arrival. Assuming this was known or measured, a result could be calculated but consisted of two ambiguous angles, mirrored on either side of the sensor's normal axis.

To avoid the requirement to know the sound pressure level at the sensor, a dual sensor assembly was created. Two sensors are co-located at an angle, and their outputs are combined through basic mathematic operations. After calibration, the sum of the sensor outputs is divided into the difference and adjusted for the offset angle used. This results in an output that follows a tangent dependence, with a unique output for each angle across a 120° range with no requirement for the sound pressure level at the sensor.

For this study, the dual sensor assembly was fabricated using two custom designed PCBs powered by a 9V battery and arranged on a 3D printed mount. The resonant frequency of the sensors in bending mode produced a 260 V/Pa output at 1.690 kHz $\pm$ 20 Hz. Experimental work was done in an anechoic chamber using an electrodynamic loudspeaker operating at resonance as a driver. Outputs were captured

using lock-in amplifiers and results manually calculated. Measurements were taken in 10° increments over an angular range of 120° with sound levels at the sensor varying from 33 dB to 54 dB. The angle error, in degrees, ranged from less than 0.3° in the region close to the normal axis (0°) to 3.4° at the outside limits of coverage, $\pm 60°$. The outcome of this research is that it is possible to operate this MEMS DF dual sensor assembly to determine the direction of a signal on resonance over an angular range of 120° with a maximum error of 3.4°.

These results represent a significant advancement in the development of a MEMS acoustic direction-finding sensor. This study has addressed the limitations of the previous generation while at the same time creating a more robust and repeatable sensor circuit board, mount, and power supply.

B. FUTURE WORK

The sensor has been made much more self-contained and reproducible than ever before. This work must continue however. Processing and calculations currently being done offline need to be incorporated into the sensor, and an improved interface needs to be developed.

It is recommended that a new PCB be designed that will hold a microprocessor and both individual sensors in one unit. The microprocessor should be chosen to allow for analog interface channels for sensor input, the required interface for result output, and a method of filtering the input signal similar to the lock-in amplifiers used in this study.

These developments should be done with consideration for follow on growth, namely incorporating three sets of sensors in an array covering 360°. Sound damping on the rear side of the sensor assembly will need to be addressed by either physical shielding or intelligent processing. Each sensor assembly will provide readings for a 120° range and be combined to produce seamless coverage.

Finally, studies should also be performed to examine the ability of the dual sensor assembly to determine the bearing of sound sources that are not located in the xz-plane.

This would help decide whether additional sensor assemblies would be needed to achieve full polar and azimuthal direction finding ability.

THIS PAGE INTENTIONALLY LEFT BLANK

APPENDIX. STANFORD RESEARCH SYSTEMS SR850 LOCK-IN AMPLIFIER SETTINGS

As outlined in [27], the Stanford SR850 Lock-In Amplifier is initially reset to factory default settings. The following coaxial wire connections are made:

- Reference In: Signal generator output

- Signal In: Sensor output

The following settings are entered into the SR850:

Ref Phase Tab

- Ref Source: External

- Ref Slope: Rising

Gain TC Tab

- Time Constant: 300 ms

Trace Scan

- Trace: 3 (R, magnitude)

- Sample Rate: 8 Hz

- Scan Length: as required to capture event

- Display Scale

- Format: Single

- Display Scale Type: Chart, trace 3 (magnitude)

THIS PAGE INTENTIONALLY LEFT BLANK

LIST OF REFERENCES

[1]   N. J. Wade and D. Deutsch, "Early binaural research," *Acoustics Today*, vol. 4, no. 3, pp. 16–27, Jul. 2003. [Online]. Available: http://deutsch.ucsd.edu/pdf/AT-2008_4_3.pdf. Accessed July 12, 2015.

[2]   T. R. Letowski and S.T. Letowski, "Auditory spatial perception: Auditory localization," *Army Research Laboratory*, 2012. [Online]. Available: http://www.dtic.mil/cgi-bin/GetTRDoc?AD=ADA562292. Accessed July 12, 2015.

[3]   X. Xiang. (2013, Mar. 13). How does the brain locate sound sources? [Online]. Available: http://knowingneurons.com/2013/03/15/how-does-the-brain-locate-sound-sources/.

[4]   R. Miles, D. Robert, and R. Hoy, "Mechanically coupled ears for directional hearing in the parasitoid fly ormia ochracea," *J. Acoust. Soc. Am.*, vol. 98, no. 6, pp. 3059-3070, Dec. 1995.

[5]   Raytheon: Boomerang III. (2015). Raytheon. [Online]. Available: http://www.raytheon.com/capabilities/products/boomerang/index.html.

[6]   Raytheon: Boomerang Warrior X. (2015). Raytheon. [Online]. Available: http://www.raytheon.com/capabilities/products/boomerang_warriorx/index.html.

[7]   Sniping at U.S. forces beginning to boomerang. (2011, Feb. 14). *Defense Industry Daily*. [Online]. Available: http://www.defenseindustrydaily.com/sniping-at-us-forces-beginning-to-boomerang-01128/.

[8]   Boomerang (countermeasure). (2015). *Wikipedia*. Available: https://en.wikipedia.org/wiki/Boomerang_(countermeasure). Accessed July 16, 2015.

[9]   EARS Gunshot Localization System. (n.d.) Qinetiq. https://www.qinetiq-na.com/wp-content/uploads/brochure_ears.pdf.

[10]   D. Quick. (2011, Mar 16). Individual Gunshot Detectors to help give U.S. soldiers a bead on enemy fire. [Online]. Available: http://www.gizmag.com/individual-gunshot-detector/18156/.

[11]   M. Touse, J. Sinibaldi, K. Simsek, J. Catterlin, S. Harrison, and G. Karunasiri, "Fabrication of a microelectromechanical directional sound sensor with electronic readout using comb fingers," *Appl. Physics Lett.*, vol. 96, no. 17, 2010.

[12]   MEMSCAP: SOIMUMPs and MEMS Multi Project Wafer Service. (n.d.).
        MEMSCAP. [Online]. Available: http://www.memscap.com
        /products/mumps/soimumps/. Accessed July 17, 2015.

[13]   Spherical Coordinate Systems. (n.d.). *Wikipedia*. Available:
        https://upload.wikimedia.org/wikipedia/commons/4/4f/3D_Spherical.svg.
        Accessed August 19, 2015.

[14]   R. Downey, "Toward a micro-scale acoustic direction-finding sensor with
        integrated electronic readout," Ph.D. dissertation, Naval Postgraduate School,
        Monterey, CA, June 2013.

[15]   J. Roth, "Integration of a high sensitivity MEMS directional sound sensor with
        readout electronics," M.S. thesis, Naval Postgraduate School, Monterey, CA,
        2009.

[16]   G. Karunasiri, "MEMS Acoustic DF Sensor," unpublished.

[17]   D. Wilmott, F. Alves, and G. Karunasiri, "MEMS Acoustic Directional Finding
        Sensor," presented at the AAAS 2015 Annual Meeting, San Jose, CA, February
        12-16, 2015.

[18]   *MS3110 Manual*, Irvine Sensors Corporation, Costa Mesa, CA, 2004.

[19]   Free Printed Circuit Board Design Software—PCB Artist. (n.d.). Advanced
        Circuits. [Online]. Available: http://www.4pcb.com/free-pcb-layout-software/.
        Accessed July 16, 2015.

[20]   CR Series datasheet. (n.d.). Panasonic. [Online]. Available:
        http://na.industrial.panasonic.com/sites/default/pidsa/files/crseries_datasheets_me
        rged.pdf. Accessed May 27, 2015.

[21]   *MS3110 Universal Capacitive Readout IC Datasheet*, Irvine Sensors Corporation,
        Costa Mesa, CA, 2004.

[22]   *522 datasheet*. Energizer Holdings, Inc. [Online]. Available:
        http://data.energizer.com/PDFs/522.pdf. Accessed May 26, 2015.

[23]   Z. Lai and J. Liu. "Effect of the microstructure of Ni/Au metallization on
        bondability of FR-4 substrate." (n.d.). Swedish Institute of Production
        Engineering Research (IVF). [Online]. Available: http://extra.ivf.se
        /ngl/documents/ChapterA/cobpaper.pdf. Accessed July 16, 2015.

[24]   *MS3110 Quick Start Setup*, Irvine Sensors Corporation, Costa Mesa, CA, 2004.

[25]   M. J. R. Lamothe and J. S. Bradley. (n.d.). Acoustical characteristics of guns as impulse sources. [Online]. Available: http://jcaa.caa-aca.ca/index.php/jcaa/article/download/541/221.

[26]   1/8-inch pressure-field microphone with Type 2670 preamplifier, 6 Hz to 140 kHz, 200V polarization. (n.d.). Brüel and Kjær. [Online]. Available: http://www.bksv.com/products/transducers/acoustic/microphones/microphone-preamplifier-combinations/4138-a-15

[27]   *Model SR850 DSP Lock-In Amplifier Manual*, Stanford Research Systems, Sunnyvale, CA, 1992.

THIS PAGE INTENTIONALLY LEFT BLANK

INITIAL DISTRIBUTION LIST

1. Defense Technical Information Center
   Ft. Belvoir, Virginia

2. Dudley Knox Library
   Naval Postgraduate School
   Monterey, California